



저작자표시-비영리-변경금지 2.0 대한민국

이용자는 아래의 조건을 따르는 경우에 한하여 자유롭게

- 이 저작물을 복제, 배포, 전송, 전시, 공연 및 방송할 수 있습니다.

다음과 같은 조건을 따라야 합니다:



저작자표시. 귀하는 원저작자를 표시하여야 합니다.



비영리. 귀하는 이 저작물을 영리 목적으로 이용할 수 없습니다.



변경금지. 귀하는 이 저작물을 개작, 변형 또는 가공할 수 없습니다.

- 귀하는, 이 저작물의 재이용이나 배포의 경우, 이 저작물에 적용된 이용허락조건을 명확하게 나타내어야 합니다.
- 저작권자로부터 별도의 허가를 받으면 이러한 조건들은 적용되지 않습니다.

저작권법에 따른 이용자의 권리는 위의 내용에 의하여 영향을 받지 않습니다.

이것은 [이용허락규약\(Legal Code\)](#)을 이해하기 쉽게 요약한 것입니다.

[Disclaimer](#)

Master of Science

**Uncertainty Quantification in Heat and Fluid Flows Around
Staggered Pin-Fin Arrays Based on Hybrid RANS/LES Model**

The Graduate School of

University of Ulsan

Department of Mechanical Engineering

Byeong-Cheon Kim

**Uncertainty Quantification in Heat and Fluid Flows Around
Staggered Pin-Fin Arrays Based on Hybrid RANS/LES Model**

Academic advisor : Professor Kyongsik Chang

A Thesis

Submitted to

the Graduate School of University of Ulsan

In partial Fulfillment of the Requirements

for the Degree of

Master of Science

by

Byeong-Cheon Kim


Department of Mechanical Engineering

University of Ulsan, Republic of Korea

August 2020

Uncertainty Quantification in Heat and Fluid Flows Around Staggered Pin-Fin Arrays Based on Hybrid RANS/LES Model

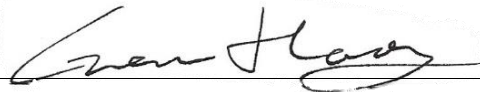
This certifies that the master thesis of Byeong-Cheon Kim is approved.



Committee Chairman Prof. Sang-Wook Lee



Committee Member Prof. Kyongsik Chang



Committee Member Dr. Geon-Hong Kim

Department of Mechanical Engineering

University of Ulsan, Republic of Korea

August 2020

Acknowledgment

Firstly, I express my appreciation to my advisor professor kyoungsik Chang. It was my huge honor to take his guidance as his student in my life. If I didn't get the opportunity that became his student, I couldn't finish the master course. Because of his supports and advice, I could be an enhanced and skilled person in every area.

I also genuinely show my gratitude to professor Sang-Wook Lee. He gave me a lot of opportunities that make me improved. In addition to that, his considerate advice made my capability more sophisticated.

I would like to thank my family member who always believes me and support me. From that support and belief, I could finish the master course and achieve my goal.

I want to thank all members of TTFL and AFDL in university of Ulsan. Especially, Yeong-Ki, Sang-Hwan, and Jae-Hyeon always helped me to everything and discussed research. I learned so many things from them. GyeongBo Kim, Ji Won Choi, GyeongBo Kim, Ji Won Choi, Gyeong-Hun Jeong, Yechan Aaron Noh, and Ga Bin Lee discussed so much. It was really helped me and motivated me a lot. I truly thanks them. I also thank Cheng Kuiyu and my Vietnam friends, Nguyen Hoai Thanh, Ho Van Thanh, Nguyen Ho Nghia, and Nguyen Khan Hoan.

Finally, I want to express my gratitude to my friend Dae-Soo Lee who walks the same way with me. The fact that he did his research best made me trying best also in my research. He is one who can discuss many things regarding the graduate student's life.

I really appreciate everyone who helped me to be here. thank you.

Abstract

Uncertainty Quantification in Heat and Fluid Flows Around Staggered Pin-Fin Arrays Based on Hybrid RANS/LES Model

In the present work, the three dimensional heat and fluid flows around staggered pin-fin arrays are predicted using two Hybrid RANS/LES, Improved Delayed Detached Eddy Simulation (IDDES) and Stress Blended Eddy Simulation (SBES) and one transitional Unsteady Reynolds Averaged Navier-Stokes (URANS) model, $k-\omega$ SSTLM. The periodic segment geometry with total 8 pins is considered with the channel height of $2D$ and the distance of $2.5D$ between each pin. The corresponding Reynolds number based on the pin diameter and the maximum velocity between pins is 10,000. Two Hybrid RANS/LES results show superior prediction in mean velocity profiles around pins, pressure distributions on the pin wall and Nusselt number distributions. However, transitional model, $k-\omega$ SSTLM show large discrepancy except in the front part where the flow is not fully developed. The two Hybrid RANS/LES models resolve the vortical structures well. Specially, SBES model is able to capture the three dimensional vortical structures after the pin. The effect of the blending function switching between RANS and LES mode of two Hybrid RANS/LES model is investigated.

The Uncertainty Quantification Forward problem is conducted with non-intrusive polynomial chaos expansion. The input variable is set as inlet velocity. It is assumed as a uniform distribution or normal distribution. Its mean μ is 3.45m/s and standard deviation σ is $\pm 0.1 \mu$. The quantity of interest is the average Nusselt number and the local Nusselt number. The results show that probability density function of output is strongly

affected by probability distribution of input.

Keywords: Staggered Pin-Fin array, Improved Delayed Detached Eddy Simulation (IDDES), Stress Blended Eddy Simulation(SBES), Hybrid RANS/LES, $k-\omega$ SSTLM, Uncertainty Quantification(UQ), Polynomial Chaos Expansion, Latin Hypercube Sampling(LHS)

Contents

Contents	i
List of Figures	iii
List of Tables.....	iv
Abbreviations	v
Chapter 1. Introduction	6
Chapter 2. Numerical Method	10
2.1 Governing Equation	10
2.2 Turbulence Models	11
2.2.1 k- ω SSTLM	11
2.2.2 Improved Delayed Detached Eddy Simulation (IDDES)	13
2.2.3 Stress Blended Eddy Simulation (SBES)	15
2.3 Discretization scheme and Coupling algorithm	16
2.3.1 Upwind scheme	16
2.3.2 Implicit discretization	17
Chapter 3. Theoretical Background for Uncertainty Quantification	19
3.1 The Definition of Uncertainty Quantification	19
3.2 Polynomial Chaos Expansion	19
3.3 Sampling Method	21
Chapter 4. Deterministic Simulations for Staggered Pin-Fin Arrays	23
4.1 Geometry	23
4.2 Grid	24
4.3 Boundary Conditions	24
4.4 Results	25

4.4.1 Grid Test	25
4.4.2 Velocity Profile	26
4.4.3 Pressure Coefficient Around The Cylinder	29
4.4.4 Nusselt Number Distribution Around The Cylinder	30
4.4.5 Pin Nusselt Number Distribution	32
4.4.6 Local Nusselt Number Distribution	33
4.4.7 Average Nusselt Number	36
4.4.8 Nusselt Number Contour	36
4.4.9 Q-Criterion	39
4.4.10 Turbulence Structure	39
4.4.11 Blending Function	42
Chapter 5. Uncertainty Quantification for Staggered Pin-Fin Arrays	44
5.1 gPCE results	44
Chapter 6. Conclusion	48
6.1 Conclusions	48
6.2 Future works	50
REFERENCES.....	51

List of Figures

Fig. 1 Pin-Fin Structure used widely	6
Fig. 2 Schematic diagram of upwind scheme	17
Fig. 3 Computational domain of geometry	23
Fig. 4 The structured mesh and the lines used to display the results. Line A (red) : end-wall normal line; line B (yellow) : pin normal line; line C (green) : line along the pin	24
Fig. 5 Boundary Conditions	25
Fig. 6 Time-averaged streamwise velocity profiles normalized by V_{max} along the line B at rows 1, 2, 3, and 5.....	28
Fig. 7 Time-averaged streamwise velocity profiles normalized by V_{max} along the line A at rows 1, 2, 3, and 5.....	28
Fig. 8 Pressure coefficient distributions along the line C in rows 1, 2, 3, and 5.....	30
Fig. 9 Nusselt number distributions along line C in rows 1, 3, and 5.....	31
Fig. 10 Averaged pin Nusselt numbers of pins along the line C.	32
Fig. 11 Local Nusselt number distributions normalized by surface average Nusselt numbers. (A) Middle line, (B) Side line.....	35
Fig. 12 Nusselt number distributions normalized by surface average Nusselt numbers. (A) Upstream region, (B) Downstream region.....	38
Fig. 13 Vortical structures around pin fin array, Q iso-surface (Q=10) colored by T_{ave} for each turbulence model.	40
Fig. 14 Time-averaged streamlines colored by T_{ave} in front of the first row of pins. HV, horseshoe vortex; SV, secondary vortex; TV, tertiary vortex; CV, corner vortex. .	41
Fig. 15 Intermittency and blending function distributions on the xz-plane at the mid-line of the y-axis	43
Fig. 16 Intermittency and blending function distributions on the xy-plane at the center height of the z-axis	43
Fig. 17 Histogram of average Nusselt number depending on the input random distribution. (A) Uniform distribution, (B) Normal distribution	45
Fig. 18 Histogram of the local Nusselt number along the middle line depending on the input random distribution. (A) Uniform distribution, (B) Normal distribution.....	47

List of Tables

Table 1. The advantages and disadvantages of the explicit scheme and implicit scheme	18
Table 2. Classical families of orthogonal polynomials	20
Table 3. Grid independence test	26
Table 4. Surface average Nusselt number	36
Table 5. The sampling points and output values	44
Table 6. The polynomial chaos coefficients depending on probability distribution of input parameter.	45

Abbreviations

CFD	Computational fluid dynamics
DES	Detached Eddy Simulation
FVM	Finite Volume Method
gPCE	Generalized Polynomial Chaos Expansion
GIS	Grid Induced Separation
IDDES	Improved Delayed Detached Eddy Simulation
LES	Large Eddy Simulation
LHS	Latin Hypercube Sampling
LLM	Log Layer Mismatch
MSD	Modelled Stress Depletion
PCE	Polynomial Chaos Expansion
PDF	Probability density function
SBES	Stress Blended Eddy Simulation
SRS	Scale Resolving Simulation
SSL	Separate Shear Layer
URANS	Unsteady Reynolds Averaged Navier-Stokes equations
UQ	Uncertainty quantification

Chapter 1. Introduction

1.1 Introduction

The pin-fin structures which are adopted in heat exchanger, nucleate reactor and turbine blade cooling system are considered as a common way to enhance the heat transfer efficiency. Even though its geometry is relatively simple, the structure of fluid and heat transfer phenomenon is complex. Therefore, many experimental or numerical research are conducted to evaluate the performance and to elucidate the fluid and heat transfer mechanism around the pin-fin structures.

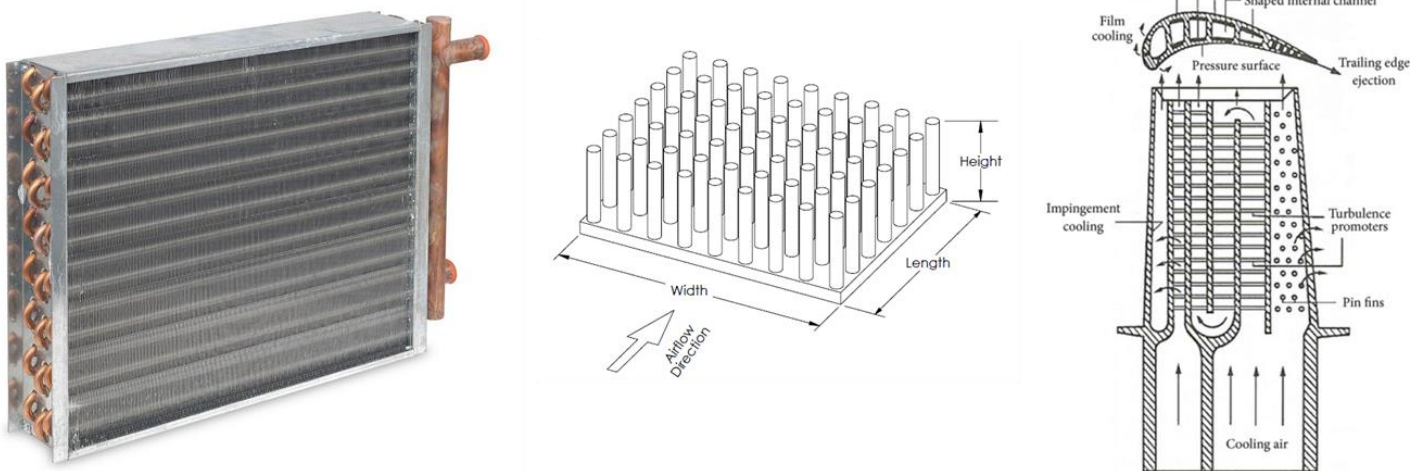


Fig. 1. Pin-Fin structure used widely

Ames et al. [1, 2, 3] conducted an experiment to study the heat transfer and fluid dynamics of staggered pin fins array using a hot wire measurement and an infrared camera at Reynolds number 3,000, 10,000 and 30,000 based on the maximum velocity between the pins. Pressure coefficient distributions, velocity distribution, and Nusselt number distribution were acquired near the cylindrical pins and off the end-walls. The experimental results showed that the turbulence augmentation along the row are major parameter for heat transfer in a staggered pin fins array. Averaged end-wall Nusselt number had a good

agreement with Metzger and Haley's correlation and Van Fossen's correlations. Ames et al. [2] also applied CFD simulations with 3D steady k- ϵ turbulence model series (standard, RNG, realizable) on the same configuration. However, they showed the limitation of steady k- ϵ turbulence models which failed to capture the unsteady vortex shedding in a staggered pin fin arrays.

Delibra and Hanjalic et al. [4, 5, 6] conducted computational fluid dynamic simulation with three kinds of turbulence models at two different Reynolds numbers 10,000 and 30,000. They used unsteady RANS model named ζ -f model, dynamic Smagorinsky subgrid-scale LES model and hybrid LES/RANS model combined with ζ -f model and dynamic Smagorinsky subgrid-scale model. The ζ -f model was able to capture the unsteady flow features caused by vortex shedding. However it showed discrepancy in resolving the wake's size and structure behind the first pin as much as LES. In view of the heat transfer, the average end-wall Nusselt number of ζ -f model's result was close to the results of LES. But both values were underpredicted to experimental results. Although a hybrid LES/RANS model used same grid with the URANS simulation, the results showed relatively better agreement than URANS results with LES and experimental results.

The study by Hao and Gorle [7] adopted a pin-fin array based on LES and k- ω SST model to perform a prior examination of selected RANS model considering discrepancies of Reynolds stress tensor. The wall-resolving LES results showed good agreement with experimental data including mean velocity, Reynolds shear stress and local averaged Nusselt number. They also found that the linear eddy viscosity model of RANS is inadequate in a complex engineering problem such as pin-fin array and provide the insight on correcting the shape of the Reynolds stress tensor through reference data from LES.

The stochastic method for heat transfer prediction based on LES and steady RANS was applied to a duct flow with pin-fin arrays by Carnevale et al.[8]. The Reynolds number was

considered as a random variable with a normal distribution. The results of LES showed the probability of a specified heat loading under a probabilistic condition. However, the results of steady RANS showed different level of uncertainty with LES. This showed that a different turbulence model result in a different level of uncertainty and that the propagation of uncertainty from epistemic uncertainty to aleatoric uncertainty is turbulence model dependent.

Recently, due to the increase of computing performance and decrease of simulation cost, scale resolving simulation (SRS) techniques are applied frequently to various engineering problems with high Reynolds number. When it is considered that Large Eddy Simulation(LES) still has some limitation in application to high Reynolds number flows which requires tremendous mesh points to resolve turbulent boundary layer appropriately, Hybrid RANS/LES can be the best alternative method to simulate turbulent heat and fluid flows. Many Hybrid RANS/LES methodologies including Detached Eddy Simulation(DES)[9] are proposed and applied to various engineering problems to show successful prediction of turbulent flows.

Menter[10] proposed the new version of a Hybrid RANS/LES model named Stress Blended Eddy Simulation (SBES) combined with the Delayed Detached Eddy Simulation(DDES) model and Improved Delayed Detached Eddy Simulation(IDDES) model. The original DES model was improved to overcome the unphysical prediction such as grid induced separation(GIS) and log-layer mismatch(LLM), which were inherent issues related with the mesh for switching between RANS and LES model in previous version of DES. The predictive capability of SBES model was evaluated through simulations of turbulent mixing layer by Frank and Menter[11] and of vertical axis wind turbine by Syawitri et al.[12]. Frank and Menter [11] simulated the turbulent mixing of two parallel planar water jets and showed that the prediction of SBES model was superior than one of

URANS $k-\omega$ SST model. The simulation of three-straight-bladed vertical axis wind turbine (VAWT) based on two grid topologies of O-type and C-type was conducted by Syawitri et al.[12] to show that SBES was able to resolve more turbulent structures like LES and the predicted power coefficient of wind turbine was more accurate than unsteady $k-\varepsilon$ realizable enhanced wall treatment results.

In the present work, heat and fluid flows around staggered pin-fin arrays are investigated using two Hybrid RANS/LES models, IDDES and SBES, and one transitional model. The adopted geometry is staggered pin-fin arrays [4] which is well known benchmark problem for evaluation of heat transfer phenomenon and Reynolds number based on the pin diameter and velocity between pins is corresponding to 10,000. We tried to evaluate the predictive capabilities of two Hybrid RANS/LES and one URANS models in convective heat transfer characteristics and flow around pin-fin arrays.

Furthermore, uncertainty quantification is conducted with non-intrusive polynomial chaos expansion. The input variable is the inlet velocity. The probability distributions of input variable are uniform distribution and normal distribution. The mean value μ is 3.45m/s and standard deviation σ is assumed as $\pm 0.1\mu$. The quantity of interest (QoI) is average Nusselt number and local Nusselt number.

Chapter 2. Numerical Methods

In this chapter, the numerical method used in the present work is explained. The SIMPLEC algorithm is used for pressure and velocity coupling. All of the spatial discretization are second order upwind scheme and unsteady term is discretized in the second order in implicit method. The time step size, Δt is set to 0.001 sec[6]. In the present work, one URANS model and two Hybrid RANS/LES models are considered; one URANS model is $k-\omega$ SST Lengtry-Menter transition model and two Hybrid RANS/LES models are IDDES and SBES models. These turbulence models are explained below.

2.1 Governing Equation

There are assumptions used in present works below.

1. All fluid is incompressible viscous flow.
2. The properties of fluid are not variable depending on the variation of temperature.
3. The gravity is not considered.

There are three governing equations (Mass conservation, Momentum conservation and Energy conservation). Considering the assumptions above, the mass conservation equation can be expressed below.

$$\frac{\partial u_i}{\partial x_i} = 0 \quad (2.1)$$

ρ is the density of fluid and \mathbf{u} is the flow velocity. Momentum conservation equation (called Navier-Stokes equation) and Energy conservation equation can be written as,

$$\frac{\partial u_i}{\partial t} + \frac{\partial(u_i u_j)}{\partial x_j} = -\frac{1}{\rho} \frac{\partial p}{\partial x_i} + \frac{\partial}{\partial x_j} \left(\nu \frac{\partial u_i}{\partial x_j} - \overline{u_i' u_j'} \right) \quad (2.2)$$

$$\rho C_p \frac{\partial T}{\partial t} + \frac{\partial u_j \rho C_p T}{\partial x_j} = \frac{\partial}{\partial x_i} k \frac{\partial T}{\partial x_j} + Q \quad (2.3)$$

where C_p is the specific heat at constant pressure. T and k is the temperature and the thermal conductivity, respectively. $-\overline{u_i' u_j'}$ is the Reynolds stress term and how to modeling this term makes the difference between the turbulence models.

2.2 Turbulence Models

2.2.1 k- ω SSTLM

The k- ω SSTLM model is proposed by Menter and Lengtry[13]. It is also known as k- ω SST γ - Re_θ model or k- ω Transition model. It includes two more transport equations relative to the original model for intermittency γ and for momentum thickness Reynolds number Re_θ . The equations are described as follow :

$$\frac{\partial(\rho\gamma)}{\partial t} + \frac{\partial(\rho u_j \gamma)}{\partial x_j} = P_{\gamma 1} - E_{\gamma 1} + P_{\gamma 2} - E_{\gamma 2} + \frac{\partial}{\partial x_j} \left[\left(\mu + \frac{\mu_t}{\sigma_\gamma} \right) \frac{\partial \gamma}{\partial x_j} \right] \quad (2.4)$$

$$P_{\gamma 1} = C_{a1} F_{length} \rho S [\gamma F_{onset}]^{C_{\gamma 3}}, E_{\gamma 1} = C_{e1} P_{\gamma 1} \gamma \quad (2.5)$$

$$P_{\gamma 2} = C_{a2} \rho \Omega \gamma F_{turb}, E_{\gamma 2} = C_{e2} P_{\gamma 2} \gamma \quad (2.6)$$

Where S is the strain rate magnitude, F_{length} is an empirical correlation that controls the length of the transition region, and C_{a1} and C_{e1} are constant values of 2 and 1, respectively. The Ω is the vorticity magnitude.

$$Re_V = \frac{\rho y^2 S}{\mu}, R_T = \frac{\rho k}{\mu \omega} \quad (2.7)$$

$$F_{onset1} = \frac{Re_V}{2193 Re_{\theta c}}, F_{onset2} = \min(\max(F_{onset1}, F_{onset1}^4), 2.0) \quad (2.8)$$

$$F_{onset3} = \max\left(1 - \left(\frac{R_T}{2.5}\right)^3, 0\right), F_{onset} = \max(F_{onset2} - F_{onset3}, 0) \quad (2.9)$$

$$F_{turb} = e^{-\left(\frac{R_T}{4}\right)^4} \quad (2.10)$$

Where y is the wall distance and $Re_{\theta c}$ is the critical Reynolds number where the intermittency first starts to increase in the boundary layer. The constants for the intermittency equation are : $C_{a1} = 2$; $C_{e1} = 1$; $C_{a2} = 0.06$; $C_{e2} = 50$; $C_{\gamma 3} = 0.5$; $\sigma_\gamma = 1$

The transport equation for the transition momentum thickness Reynolds Re_θ is

$$\frac{\partial(\rho Re_\theta)}{\partial t} + \frac{\partial}{\partial x_j}(\rho u_j Re_\theta) = P_{\theta t} + \frac{\partial}{\partial x_j} \left[\sigma_{\theta t} (\mu + \mu_t) \frac{\partial}{\partial x_j} (Re_\theta) \right] \quad (2.11)$$

$$P_{\theta t} = C_{\theta t} \frac{\rho}{t} (Re_{\theta t} - Re_\theta) (1.0 - F_{\theta t}), t = \frac{500\mu}{\rho U^2} \quad (2.12)$$

$$F_{\theta t} = \min \left[\max \left\{ F_{wake} e^{\left(\frac{-y}{\delta}\right)^4}, 1.0 - \left(\frac{\gamma - 1/50}{1.0 - 1/50}\right)^2 \right\}, 1.0 \right] \quad (2.13)$$

$$\theta_{BL} = \frac{Re_{\theta} \mu}{\rho U}, \delta_{BL} = \frac{15}{2} \theta_{BL}, \delta = \frac{50 \Omega y}{U} \delta_{BL}, Re_{\omega} = \frac{\rho \omega y^2}{\mu} \quad (2.14)$$

$$F_{wake} = e^{-\left(\frac{Re_{\omega}}{1E5}\right)^2} \quad (2.15)$$

The model constants for the Re_{θ} equation are : $C_{\theta t} = 0.03$; $\sigma_{\theta t} = 2.0$; the empirical correlation used in this model is based on the pressure gradient coefficient λ_{θ} and turbulent intensity Tu .

$$Tu = \frac{100}{U} \sqrt{\frac{2}{3} k}, \lambda_{\theta} = \frac{\theta^2}{\nu} \cdot \frac{dU}{ds} \quad (2.16)$$

$$Re_{\theta t} = \begin{cases} \left[1173.51 - 589.428 Tu + \frac{0.2196}{Tu^2} \right] F(\lambda_{\theta}) & Tu \leq 1.3 \\ 331.50 [Tu - 0.5658]^{-0.671} F(\lambda_{\theta}) & Tu > 1.3 \end{cases} \quad (2.17)$$

$$F(\lambda, Tu) = \begin{cases} 1 - [-12.986 \lambda_{\theta} - 123.66 \lambda_{\theta}^2 - 405.689 \lambda_{\theta}^3] e^{-\left(\frac{Tu}{1.5}\right)^{1.5}} & \lambda_{\theta} \leq 0 \\ 1 + 0.275 [1 - e^{[-35.0 \lambda_{\theta}]}] e^{\left[\frac{-Tu}{0.5}\right]} & \lambda_{\theta} > 0 \end{cases} \quad (2.18)$$

2.2.2 Improved Delay Detached Eddy Simulation (IDDES)

The IDDES model [16] combines the DDES model [17] and the wall-modelled LES (WMLES) model [18, 19]. The original DES model proposed by Spalart et al.[17] and Menter [20] is known to be abnormally sensitive to mesh resolution, which determines the length scale between the RANS model and the sub-grid scale model. If the change of grid

density is abrupt or if the mesh is not refined enough for a WMLES, the modelled turbulence and eddy viscosity decreases. This phenomenon is called modelled stress depletion (MSD), which causes early unphysical separation termed grid-induced separation (GIS) [17]. The GIS deteriorates the solution near the regions between the RANS mode and the LES mode. Moreover, the DES model shows a relatively strong logarithmic layer mismatch (LLM) between the inner RANS and the outer LES. This issue of LLM is also shown in the DDES model, and the IDDES model has a feature to switch the turbulence length scale in the dissipation term of the turbulent kinetic energy equation :

$$\frac{\partial(\rho k)}{\partial t} + \nabla \cdot (\rho \mathbf{u}k) = \nabla \cdot [(\mu + \sigma_k \mu_k) \nabla k] + P_k - \rho \sqrt{k^3} / l_{IDDES} \quad (2.19)$$

$$l_{IDDES} = \tilde{f}_d \cdot (1 + f_e) \cdot l_{RANS} + (1 - \tilde{f}_d) \cdot l_{LES} \quad (2.20)$$

$$l_{LES} = C_{IDDES} \Delta, l_{RANS} = \frac{\sqrt{k}}{C_\mu \omega} \quad (2.21)$$

$$\Delta = \min \{ C_\omega \max[d_w, h_{max}], h_{max} \} \quad (2.22)$$

Where Δ is the LES length scale and h_{max} is the maximum edge length of the cell. d_w denotes the distance from the wall.

$$\tilde{f}_d = \max\{(1 - f_{dt}), f_b\}, \quad f_{dt} = 1 - \tanh[(C_{dt1} \cdot r_{dt})^{C_{dt2}}] \quad (2.23)$$

$$r_{dt} = \frac{v_t}{\kappa^2 d_w^2 \sqrt{0.5(S^2 + \Omega^2)}}, r_{dl} = \frac{v}{\kappa^2 d_w^2 \sqrt{0.5(S^2 + \Omega^2)}} \quad (2.24)$$

$$f_b = \min\{2\exp(-9\alpha^2), 0\}, \alpha = 0.25 - \frac{d_w}{h_{max}} \quad (2.25)$$

$$f_e = f_{e2} \cdot \max((f_{e1} - 1.0), 0) \quad (2.26)$$

$$f_{e1} = \begin{cases} 2\exp(-11.09 \cdot \alpha^2) & \text{when } \alpha \geq 0 \\ 2\exp(-9 \cdot \alpha^2) & \text{when } \alpha < 0 \end{cases} \quad (2.27)$$

$$f_{e2} = 1 - \max(f_t, f_l)$$

$$f_t = \tanh\left(\left(C_t^2 \cdot r_{dt}\right)^3\right), f_l = \tanh\left(\left(C_l^2 \cdot r_{dl}\right)^3\right) \quad (2.29)$$

f_{dt} is the empirical function for shielding of the DDES model from MSD, which is similar to f_d in the DDES model. ν and ν_t are the molecular and eddy viscosity, respectively. S and Ω are the strain rate and vorticity tensor. Detailed formulations and related constants can be found in Gritskevich et al. [16]

2.2.3 Stress Blended Eddy Simulation (SBES)

An SBES turbulence model was proposed by Menter [10] considering the ability to blend the RANS model directly into LES model based on the same shielding function f_{SDES} of the SDES model.[14] Menter[10] recommended this method, “Automatic Zonal Modeling,” to satisfy 1) a high degree asymptotic shielding of the RANS boundary layer under mesh refinement, 2) reliable and swift switching from RANS to LES in separate shear layers (SSLs), 3) operation in WMLES mode, 4) able to combine all RANS and all LES models, and 5) robustness even on non-perfect industrial meshes [10]. The equation for blending of stress tensors can be expressed as :

$$\tau_{ij}^{SBES} = f_{SDES}\tau_{ij}^{RANS} + (1 - f_{SDES})\tau_{ij}^{LES} \quad (2.30)$$

where τ_{ij}^{RANS} is the RANS Reynolds stress tensor and τ_{ij}^{LES} is the LES stress tensor. In the case of the eddy viscosity model, the formulation above simplifies to :

$$\mu_t^{SBES} = f_{SDES}\mu_t^{RANS} + (1 - f_{SDES})\mu_t^{LES} \quad (2.31)$$

When f_{SDES} is zero, the RANS model is applied; when the f_{SDES} is 1, the algebraic LES model is applied. In the present work, the two-equation model ($k-\omega$ SST) is used for the RANS model, and the Wall-Adapting Local Eddy-viscosity (WALE) model is adopted for the LES model. The SBES model can switch from the RANS model to LES faster than the other hybrid RANS/LES models in separate layers since the level of turbulence stress of the LES model in the RANS boundary layer is low. As a result, the solution is more realistic and consistent.

2.3 Discretization Schemes and Coupling Algorithm

2.3.1 Upwind Scheme

An upwind scheme is one of the discretization schemes for convection-diffusion term in Navier-Stokes equation and Energy conservation equation. there are a lot of numerical schemes for the discretization of the convection-diffusion term in finite volume method (FVM). For example, central scheme, upwind scheme, hybrid scheme and QUICK etc are representative. Especially, upwind scheme has been wildly used as a spatial discretization scheme.

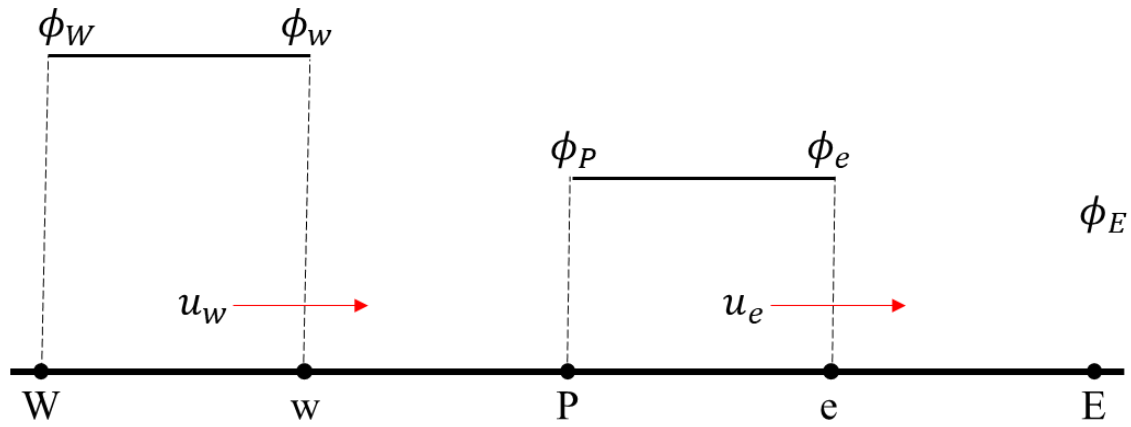


Fig. 2. Schematic diagram of Upwind scheme

Fig.2 shows the nodal values used to calculate cell face value. ϕ is the value of a property. If u_w and u_e have a positive value, $\phi_w = \phi_W$ and $\phi_e = \phi_P$. It is different with central scheme; ($\phi_w = \frac{\phi_P + \phi_W}{2}$, $\phi_e = \frac{\phi_E + \phi_P}{2}$). Therefore upwind scheme can identify the flow direction that the central scheme can't identify. In other words, transportiveness is built. In addition to transportiveness, the simplicity of upwind scheme is the reason why it has been widely applied in CFD calculations.

2.3.2 Implicit Discretization Scheme

There are two methods of discretization for the rate of change term. One is the Explicit method and the other is the Implicit method. Each method has advantages and disadvantages.

First of all, Explicit scheme has the advantage to write code easily because of the simplicity. But it has a stability problem. Therefore the time step size is limited. This limitation induces long computation time. The higher dimension is considered, the more strict stability criteria are needed to satisfy. In addition to the stability problems, the time lag occurs at boundary conditions.

On the other hand, the Implicit scheme is unconditionally stable. That's why it solves the matrix equation at every time step. It takes more time to solve the one time step than the explicit scheme takes. However total computation time is shorter than the explicit scheme. Its solution converges with a large time step size. But if the time step size is too large, the truncation error contaminates the solution. Table.1 shows the advantages and disadvantages of the explicit scheme and implicit scheme.

Table 1. *The advantages and disadvantages of the explicit scheme and implicit scheme*

	Advantages	Disadvantages
Explicit Scheme	<ul style="list-style-type: none"> • Easy to write code 	<ul style="list-style-type: none"> • Limitation of time step size due to stability problem • The higher dimension is considered, the more strict stability criteria are needed to satisfy • Time lag at boundary condition
Implicit Scheme	<ul style="list-style-type: none"> • Unconditionally stable 	<ul style="list-style-type: none"> • Difficult to write code • Taking more time than explicit scheme for one time step

Chapter 3. Theoretical Background for Uncertainty Quantification

3.1 The Definition of Uncertainty Quantification

The uncertainty quantification is the mathematical method that deals with quantitative characterization and the reduction of uncertainties in applications. Uncertainty quantification is used for robust design/optimization, model validation, and certification for high-risk decisions.

Uncertainty means that there is not certain value for a specific parameter. because of the physical variation of the value and the lack of accuracy in calculation and measurement. There are two categories to classify the type of uncertainty. One is aleatory uncertainty and the other is epistemic uncertainty. Aleatory uncertainty is induced by natural variabilities in the real system. therefore it is impossible to be reduced or eliminated. For examples of aleatory uncertainty are material properties, noise, etc. Epistemic uncertainty is induced by the lack of knowledge of physics. and it is caused by the modeling hypothesis. So it is possible to be reduced or eliminated. For examples of epistemic uncertainty are turbulence model, boundary conditions, etc.

3.2 Polynomial Chaos Expansions

The Polynomial chaos expansions (PCE) is non-intrusive method to determine propagation of uncertainty in dynamic system when there is probabilistic uncertainty in the system parameters. It allows one to represent a random output as a polynomial series in the input variables. The generic problem can be described like below :

$$y = f(x) \tag{3.1}$$

f is the computational model and in the present research, it is the Navier-Stokes equation. x is the input parameter. y is the output referred to Quantity of interest (QoI). As input parameter x is a random variable, the equation is modified like below :

$$Y = f(X) \quad (3.2)$$

Y and X are expressed as random variables. If the assumption that the output random variable has finite variance is applied, the equation (3.2) is modified as follow :

$$Y = \sum_{n=0}^{\infty} \alpha_n(X) \Psi_n(\xi_j) \quad j = 0, 1, 2, \dots, P \quad (3.3)$$

Where $\alpha_n(X)$ are the polynomial chaos coefficients and Ψ_n is an element of an orthogonal family. This correspondences between the random variable distribution and orthogonal polynomial family are shown in Table.2.

Table 2. *Classical families of orthogonal polynomials*

Type of variable	Distribution	Orthogonal polynomials	Hilbertian basis $\Psi_n(\xi)$
Uniform $U(-1,1)$	$\frac{1(\xi)}{2}$	Legendre $P_n(\xi)$	$P_n(\xi) / \sqrt{\frac{1}{2n+1}}$
Gaussian $G(0,1)$	$\frac{1}{\sqrt{2\pi}} e^{-\xi^2/2}$	Hermite $H_n(\xi)$	$H_n(\xi) / \sqrt{n!}$
Gamma $\Gamma(a, \lambda = 1)$	$x^a e^{-\xi}$	Laguerre $L_n^a(\xi)$	$L_n^a(\xi) / \sqrt{\frac{\Gamma(n+a+1)}{n!}}$
Beta $B(a, b)$	$1(\xi) \frac{(1-\xi)^a (1+\xi)^b}{B(a)B(b)}$	Jacobi $J_n^{a,b}(\xi)$	$J_n^{a,b}(\xi) / \mathfrak{S}_{a,b,n}$

ξ are a vector of random variables representing the system's uncertainties. the random variable ξ is randomly sampled in accordance with its statistical distribution equation above represents a system of $P + 1$ equations in $P + 1$ unknowns. As a system of linear equations, the equation (3.3) can be solved for the α_n . A linear system can be obtained as follow :

$$\begin{bmatrix} \Psi_0(\xi_0) & \Psi_0(\xi_0) & \dots & \Psi_P(\xi_0) \\ \Psi_0(\xi_1) & \Psi_0(\xi_1) & \dots & \Psi_P(\xi_1) \\ \vdots & \vdots & \ddots & \vdots \\ \Psi_0(\xi_{P-1}) & \Psi_1(\xi_{P-1}) & \dots & \Psi_P(\xi_{P-1}) \\ \Psi_0(\xi_P) & \Psi_1(\xi_P) & \dots & \Psi_P(\xi_P) \end{bmatrix} \begin{bmatrix} \alpha_0 \\ \alpha_1 \\ \vdots \\ \alpha_{P-1} \\ \alpha_P \end{bmatrix} = \begin{bmatrix} Y_1 \\ Y_2 \\ \vdots \\ Y_{P-1} \\ Y_P \end{bmatrix} \quad (3.4)$$

If the more than $P + 1$ samples are chosen, then the over-determined system of equations should be solved using the least square method.

The maximum number of terms, $P + 1$, may be computed from the formula

$$P + 1 = \frac{(p + n)!}{p! n!} \quad (3.5)$$

p is the order of the polynomial set used for the chaos.

3.3 Sampling Method

Latin Hypercube Sampling (LHS) method is the one of the sampling method and it is proposed by McKay et al. [24] LHS is developed to improve the computational efficiency and the global accuracy of approximation. The key to this method is stratification of the input probability distribution. Stratification divides the cumulative curve into equal interval. A sample is then randomly taken from each interval or “stratification”.

Hosder et al. [25] investigated the effects on the results by the number of collocation points in a systematic way through the introduction of a parameter, the oversampling rate

n_p defined below.

$$n_p = \frac{\textit{the number of samples}}{P + 1} \quad (3.5)$$

Oversampling rate $n_p = 2$ yields a better approximation to the statistic at each polynomial degree.

Chapter 4. Deterministic Simulations for Staggered Pin-Fin Arrays

4.1 Geometry

The geometry in the present work is adopted from the experiments of Ames et al. [1, 2, 3], which consists of multiple pins attached at the plane. The cylindrical pins with diameter $D = 0.0254$ m are located in a staggered array with a distance of $2.5D$ between each pin and each row of pins. The channel height is set to $2D$. For efficient simulation, the periodic segment geometry is considered, which is the same as in simulations by Delibra et al. [4, 5, 6] The spanwise length of the channel is $2.5D$ and the first row of pins is set to $7.5D$ away from the inlet for development of boundary layers on end-walls. The distance between the last row of pins and the outlet is also $7.5D$ to retain a fully developed exit flow for better numerical convergence. The total length in the streamwise direction is $32.5D$. Details of the geometry and computational domain are shown in Fig. 3.

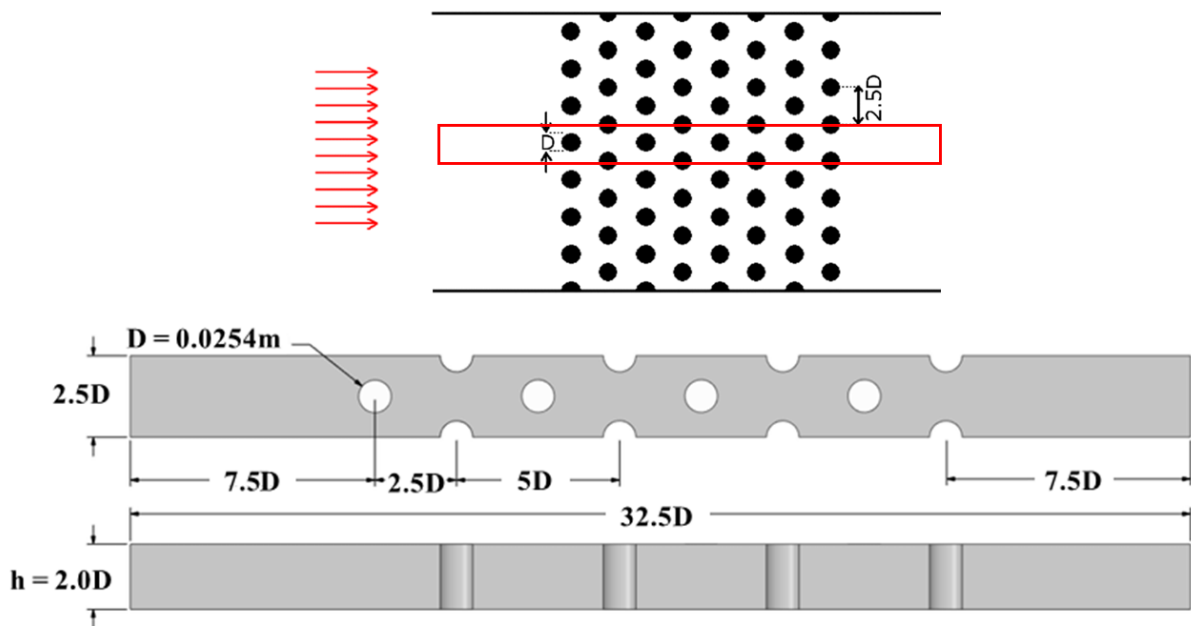


Fig. 3. Computational domain of geometry

4.2 Grid

The grid is generated with hexahedral mesh in multi-blocks using ANSYS ICEM CFD. [15] To resolve the turbulent boundary layer near the wall at the bottom and the cylinder pins, 10 layers of mesh are inserted off the wall. The first grid height off the wall is set to satisfy the wall unit within 1.0, which is averaged in the computational domain. The total number of cells corresponds to 14,043,965. The grid system adopted in the present simulation is shown in Fig. 4.

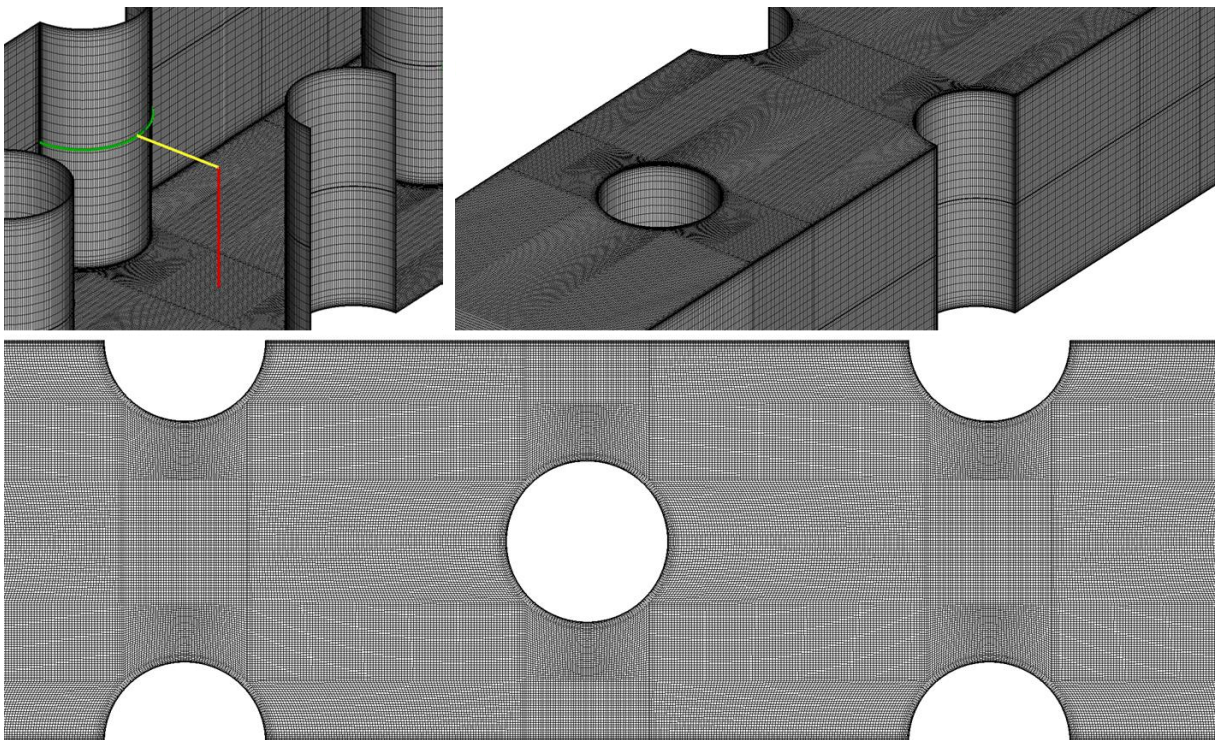


Fig. 4 The structured mesh and the lines used to display the results.
Line A (red) : end-wall normal line; line B (yellow) : pin normal line; line C (green) : line along the pin.

4.3 Boundary Conditions

The Reynolds number, which is based on the diameter D and the averaged velocity V_{max} at the minimum passage, is 10,000. The turbulent intensity of the inflow is set to 1.5%,

the same as in the experimental conditions of Ames et al. [1, 2, 3] and the numerical simulations of Hao and Gorle. [7] The periodic boundary conditions are applied on both side surfaces, and the pressure outlet conditions are at the outlet. At the end wall and pin wall, the same constant temperature condition is applied as in Delibra et al. [4, 5, 6]. The temperature difference ΔT ($\Delta T = T_{wall} - T_{in}$) between the inlet temperature T_{in} and the wall temperature T_{wall} is set to 25 K. The boundary conditions are considered in this research are shown in Fig. 5.

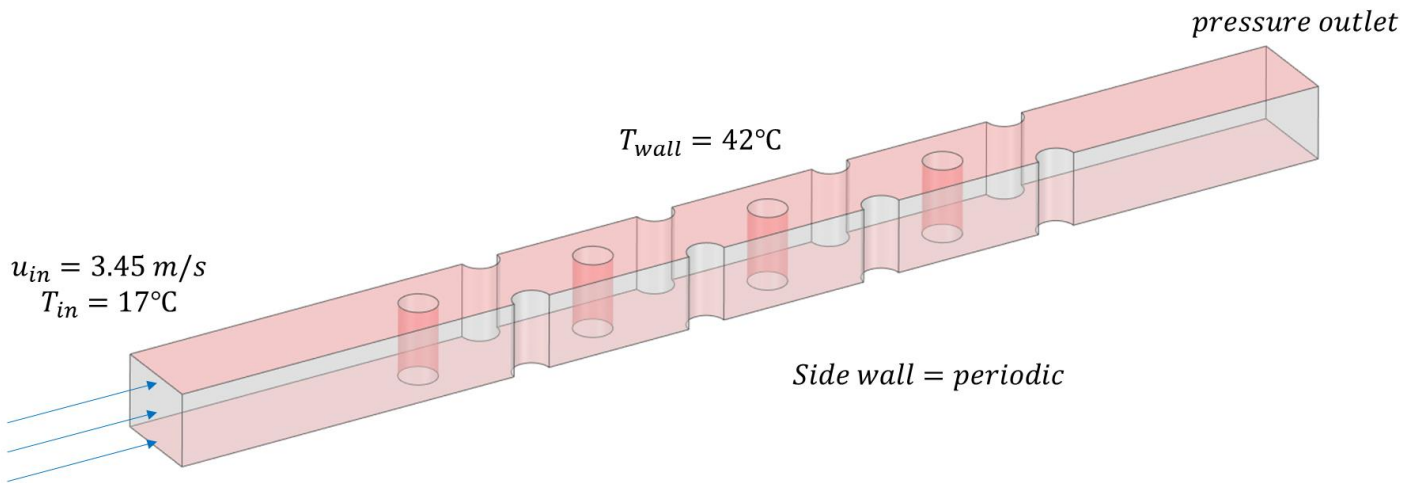


Fig. 5. *Boundary Conditions*

4.4 Results

4.4.1 Grid test

The grid test is achieved using coarse (10 million cells), medium (14 million cells), and fine mesh (20 million cells), which is shown in Table. 3, based on the adopted hybrid RANS/LES models, IDDES and SBES. To resolve the turbulent boundary layer, the first off-wall point is set to less than the wall unit, 1.0 in all meshes. The averaged Nusselt number, which is calculated through averaging from inlet to outlet, is compared for the grid test. In both models the averaged Nusselt number decreases as the number of elements

increases, but the result of SBES is closer to the reference value and LESs other than the IDDES model. Further, the differences between the coarse mesh and fine mesh are about 8.2% and 7.2% in the IDDES and SBES model, respectively, which means the dependency of the mesh is higher in IDDES than in SBES. Thus, the medium grid with 14 million cells is selected as appropriate given the associated computational time and cost.

Table 3. *Grid independence test*

Nu_{ave}	Coarse	Medium	Fine
Number of cells	10,165,687	14,043,965	20,564,381
IDDES	45.11	43.46	41.54
SBES	46.74	44.61	43.47

4.4.2 Velocity profiles

Fig.6 shows the mean velocity profiles normalized by V_{max} along the line between a certain row of pins (at 90°) at the middle height plane ($z/D = 1.0$). The velocity profiles are averaged in enough time (~6,000 time steps) to obtain statistically steady solutions in every model. The experimental data by Ames et al. [1, 2, 3] are denoted by the diamond symbol; the two CFD results by Delibra et al. [4, 5, 6] are the LES data (solid black line) and the URANS data (black dashed line) for comparison with the present results. The other three lines (green, blue, and red) correspond to the present results: k- ω SSTLM, IDDES, and SBES, respectively. In the first row all of the simulation results are in good agreement with the experimental data. In the other rows the two hybrid RANS/LES models agree well with the LES results (row 5) and the experimental data (rows 1, 2, and 3), but the ζ -f

URANS [5] and $k-\omega$ SSTLM models predict different velocity profiles with large discrepancies, specially near the center between the pins.

The mean velocity profiles along the perpendicular line on the end-wall are plotted in Fig. 7. The turbulent boundary layer profile, which was obtained from other simulations in the corresponding channel geometry with up-and-down walls, was fed at the inlet of the computational domain, the three present results show discrepancies with other reference data in the first row. However, the boundary layer of the two hybrid RANS/LES models was developed appropriately and follows the tendency of the experimental data. In the second row, IDDES and SBES show magnitudes of velocity similar to the experimental data, but the URANS and LES models show less velocity. In the third row the SBES result is closer to the LES results and the experiment data than are the IDDES and other URANS models. Finally, the velocity profiles of IDDES and SBES agree well with the LES profile. In every row the two URANS models produced large discrepancies with the reference data

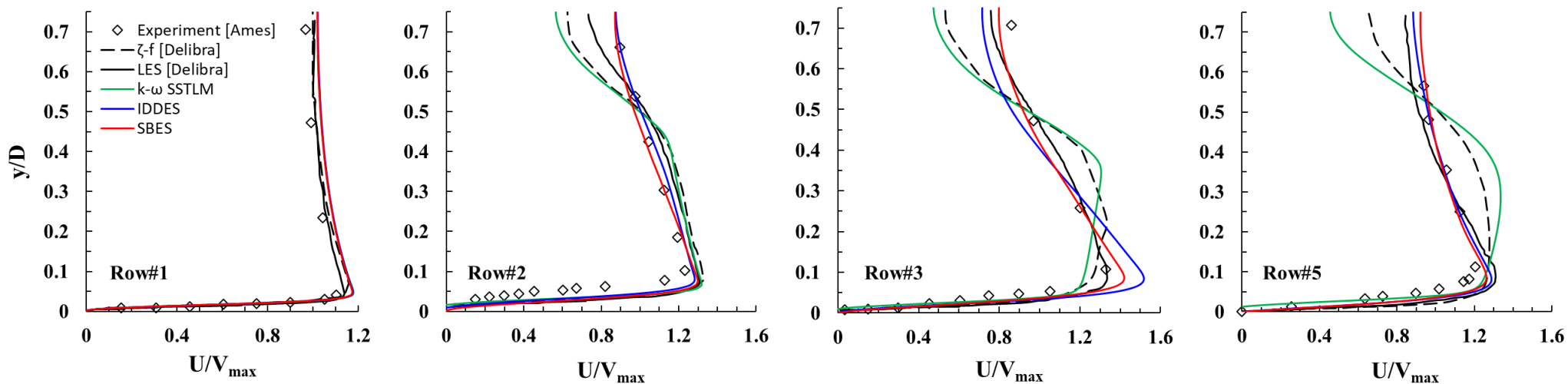


Fig. 6. Time-averaged streamwise velocity profiles normalized by V_{max} along the line B at rows 1, 2, 3, and 5.

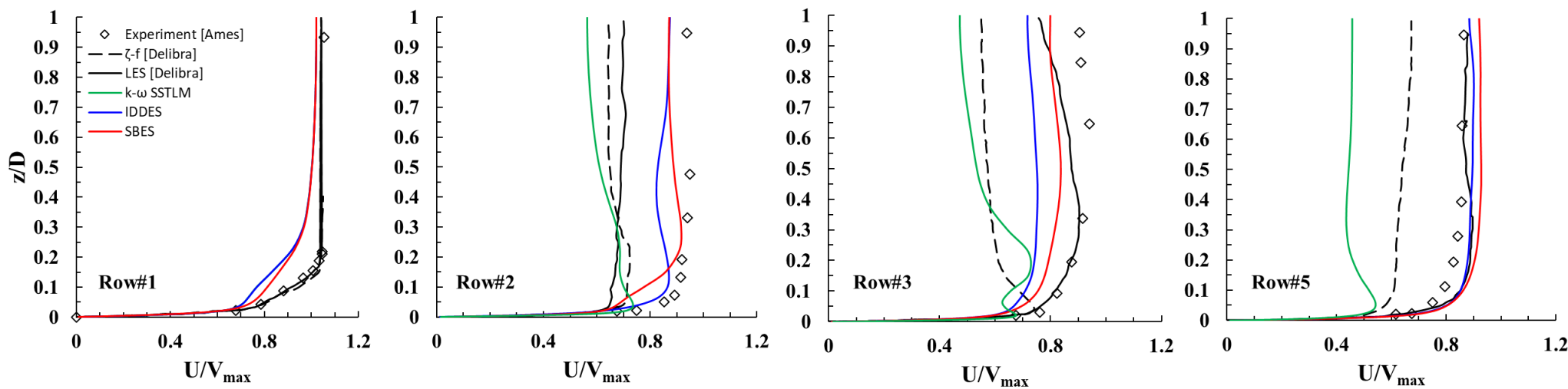


Fig. 7. Time-averaged streamwise velocity profiles normalized by V_{max} along the line A at rows 1, 2, 3, and 5.

4.4.3 Pressure coefficient around the cylinder

The averaged pressure coefficients around the pins for rows 1, 2, 3, and 5 are plotted in Fig. 8. Every model shows consistent predictions of the pressure coefficient at the first and second row, but there are some discrepancies in the other two rows. At the third row, the difference between each model is largest and the predictions of the two LES models by Delibra et al. [4] and Hao and Gorle [7] are closest to the experimental data. In the present work the SBES model shows predictions closest to the reference data, and the two LES models and the $k-\omega$ SSTLM model have patterns similar to the ζ -f model by Delibra et al. [5]. At the fifth row, even though each model shows a similar prediction in the region of the attached flow and after the separation point, there is large discrepancy between $\theta = 50^\circ$ and 100° in the prediction of each model. Delibra et al. [5] showed that the ζ -f model's pressure coefficient prediction at the fifth row was better than the LES model's, which is shown in Fig. 8. They mentioned that this was not in conflict with the excellent LES predictions of the mean velocity in the cross section, since this agreement did not guarantee the accurate prediction in the pin wakes. The LES model by Hao and Gorle [7] best predicted this coefficient in the fifth row, even though that model had a slower pressure recovery (with a maximum difference of 13%) among all the models considered in the present work. The predictions of the two hybrid RANS/LES models in the present work are between the results of the two LES models

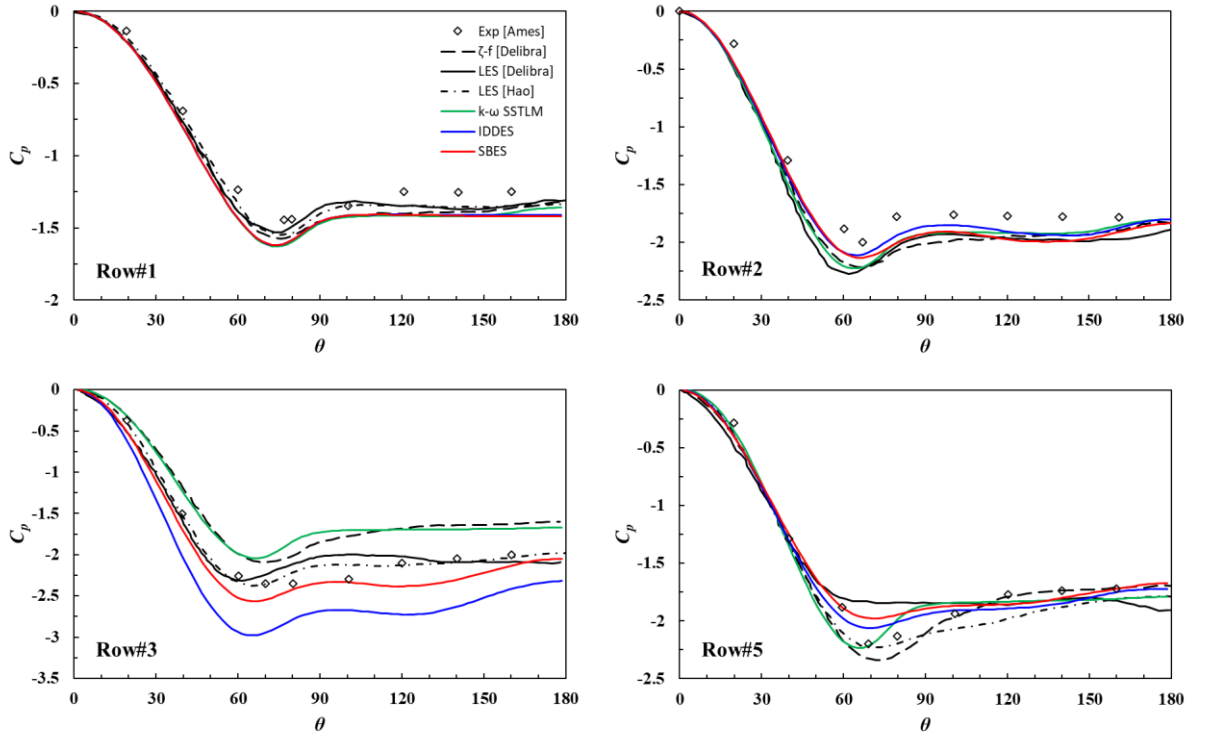


Fig. 8. Pressure coefficient distributions along the line C in rows 1, 2, 3, and 5.

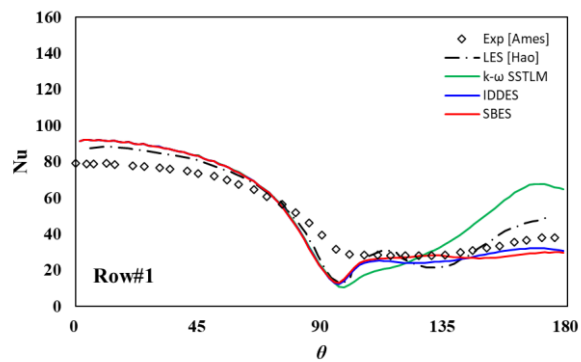
4.4.4 Nusselt number distribution around the cylinder

Fig. 9 shows the distributions of the Nusselt numbers around the pins for rows 1, 3, and 5. The Nusselt number is calculated using the expression

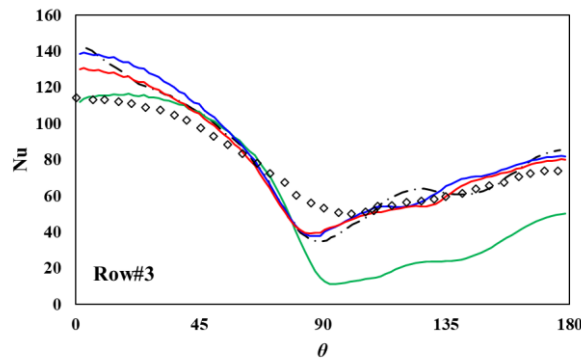
$$Nu = qD/k(T_b - T_{in}) \quad (4.1)$$

where q and k are the wall normal heat flux and thermal conductivity, respectively, and T_b is the bulk-flow temperature. The Nusselt number distribution shows the highest value at the leading edge of each pin and decreases along the pin surface; after separation the value plateaus or increases gradually. The results of IDDES and SBES agree well with the experimental data and the LES results of Hao and Gorle [7] in the whole region. The IDDES and SBES models overestimate the Nusselt number at the leading edge, the same

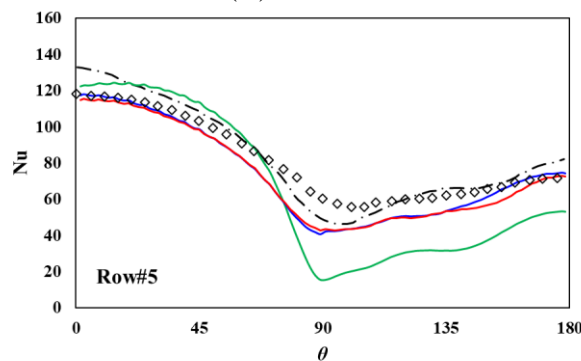
as with LES model. The difference from the experimental data is about 10% at row 1 and about 10% and 15% for SBES and IDDES, respectively, at row 3. All the numerical models fail to predict the minimum Nusselt number just upstream of the separation points. Hao and Gorle explain that this difference is due to a non-uniformity of the pin surface temperature in the experiment (rows 1, 2, and 3). However, there is a somewhat large discrepancy in the prediction of the $k-\omega$ SSTLM model, especially in the region after the separation.



(A) Row 1



(B) Row 3



(C) Row 5

Fig. 9. Nusselt number distributions along line C in rows 1, 3, and 5.

4.4.5 Pin Nusselt number distribution

In Fig. 10 the predicted Nusselt number around each pin is averaged over the surface and plotted for a total of eight pins. Experimental data and LES results by Hao and Gorle [7] are presented for comparison with the present results. The averaged Nusselt number for each pin increases until the fourth row and then stays constant after a small decrease. The results of IDDES and SBES are fairly consistent with each other and agree well with other reference data until the third row. The predicted Nusselt number decreases after third row and then stays constant with a maximum difference of 9% from the experimental data. There is still a large discrepancy in the $k-\omega$ SSTLM model even though the unsteady temperature and velocity field are averaged in time over enough time. This discrepancy comes from the failure of the correct thermal boundary layer on the pin surface wall.

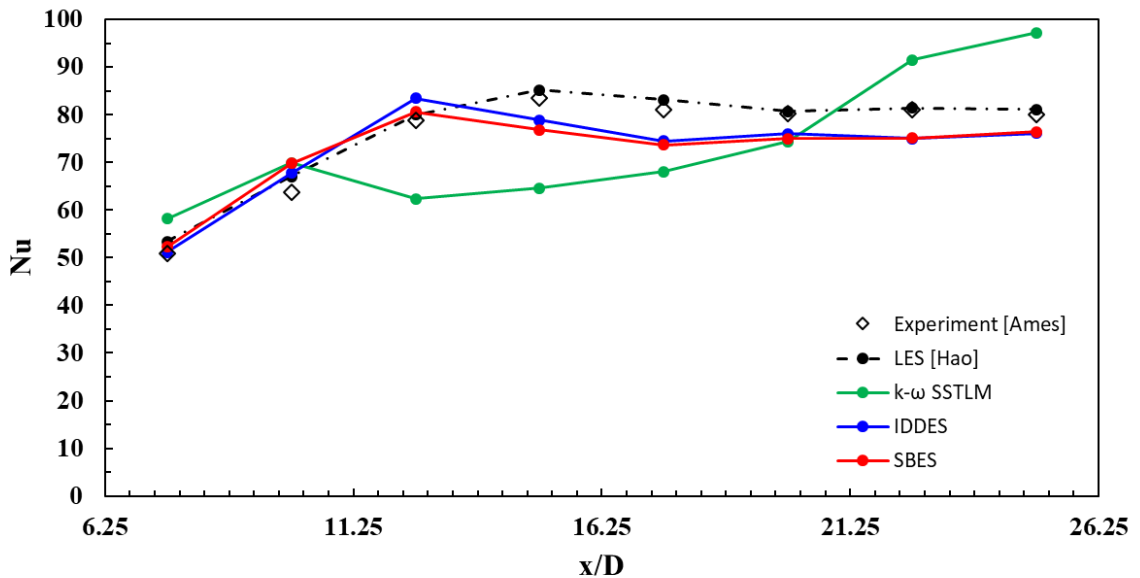


Fig. 10 Averaged pin Nusselt numbers of pins along the line C.

4.4.6 Local Nusselt number distribution

Fig. 11 shows the local Nusselt numbers normalized by averaged Nusselt numbers along the middle line (A) and the side line (B) on the end-wall. For clear recognition of the calculated local Nusselt numbers, the results of the present work are plotted in the same colors as in the other figures. In previous research, most of the URANS models failed to predict the local Nusselt number distributions similarly with experimental results (rows 1, 2, and 3), whereas some LES models were able to follow the shape of the distribution of the local Nusselt numbers (row 5). The two hybrid RANS/LES results show superior prediction similar to the previous LES results and experiment data. The Nusselt number shows an abrupt increase near the upstream wall of each pin, and a gradual decrease after the downstream wall of a pin. IDDES and SBES were able to predict these behaviors well and agreed well with the LES results. However, the values predicted by the two hybrid RANS/LES models are underestimated compared to the reference values as the flow goes downstream. This underestimation comes from the lack of resolving the vortex shedding after the pins. On the other hand, the LES model resolves enough vortex structures by having enough mesh and inherent model characteristics.

The $k-\omega$ SSTLM model is not able to follow the variation of local Nusselt numbers in most of the regions, which is consistent with the results of $k-\omega$ SSTLM modeling by Carnevale et al. [8] Benhamadouche et al. [22] investigated the assessment of three URANS models (EB-RSM, $k-\omega$ SST, and ϕ -model) and a LES model in the present geometry, and determined that the $k-\omega$ SST and the ϕ -model (a stabilized version of the v^2-f model) underestimated Nusselt numbers after the first few pins where the turbulence was not yet fully developed and mixing was dominant. Since the $k-\omega$ SSTLM model is a transitional model rather than a fully developed turbulent one, its prediction of Nusselt

numbers after the first pin is slightly better than the other two fully developed turbulent models investigated by Benhamadouche et al. [22] However, there are still large discrepancies in the other pins, which show behavior similar to the results of the ϕ -model.[22]

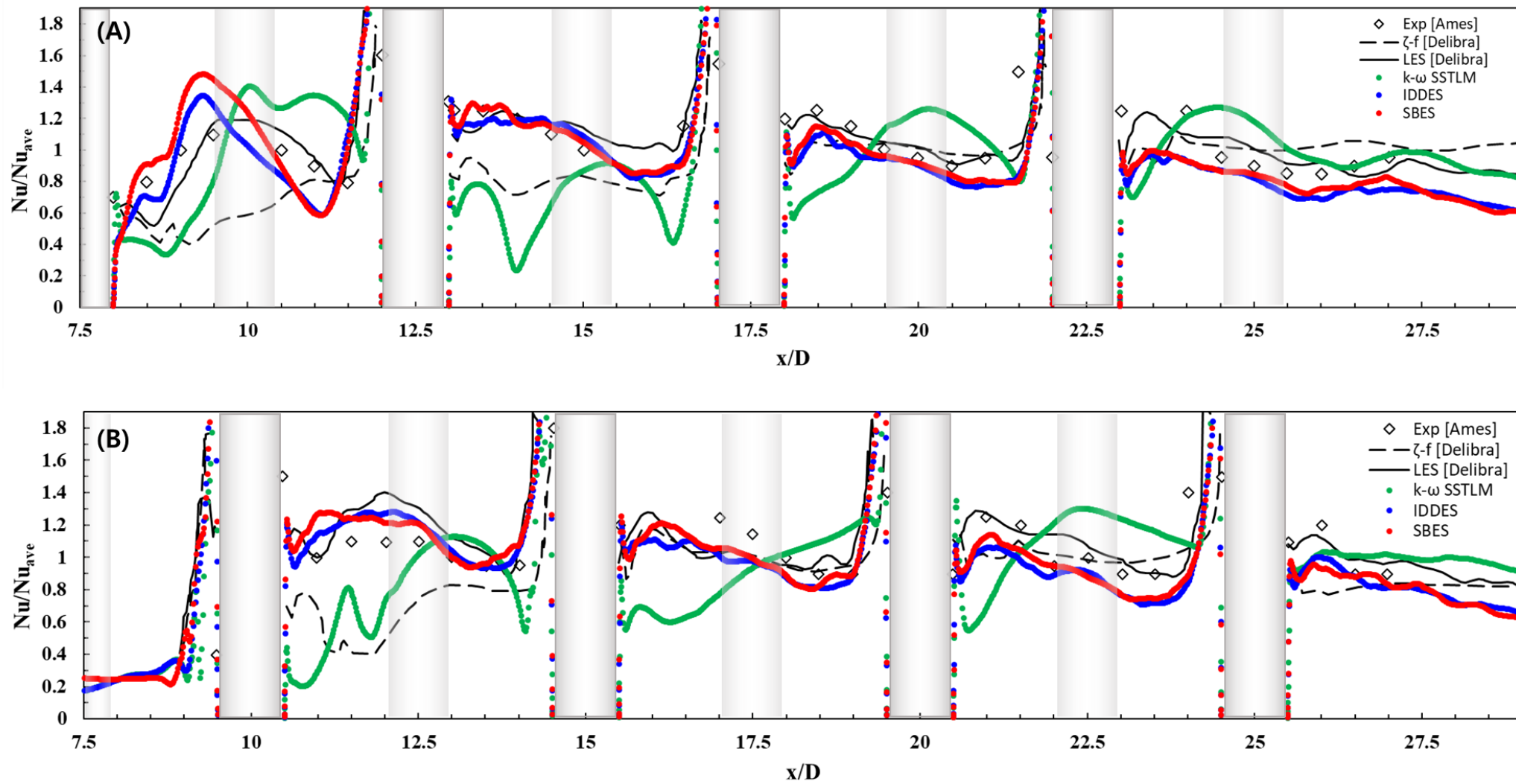
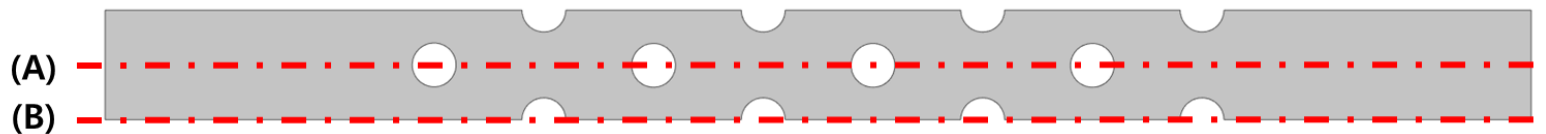


Fig. 11. Local Nusselt number distributions normalized by surface average Nusselt numbers. (A) Middle line, (B) Side line

4.4.7 Average Nusselt number

Table. 4 summarizes the averaged end-wall Nusselt numbers of the considered models and the reference data. The predicted Nusselt numbers on the end-wall are 44.6, 43.5, and 41.3 by SBES, IDDES, and k- ω SSTLM, respectively. Even though these values are about 20% discrepant from the experimental data [3], they are similar to the values predicted by other numerical simulations, LES [4] and hybrid RANS/LES. Delibra et al. [4, 5, 6] mentioned that deviations between experimental data and numerical simulation are caused by heat escape by radiation and/or heat sink in the experiment. Although numerical simulations do not consider this effect, an LES model with about 11 million mesh cells by Hao and Gorle [7] predicted the averaged end-wall Nusselt number as 53.5, within 1% of the experimental data result.

Table 4. *Surface average Nusselt number*

	k-ω SSTLM	IDDES	SBES		
Nu_{ave}	41.3	43.5	44.6		

	Experiment [Ames]	ζ - f [Delibra]	LES [Delibra]	Hybrid URANS/LES [Delibra]	LES [Zengrong Hao]
Nu_{ave}	54.1	46.2	44.3	45.3	53.5

4.4.8 Nusselt number Contour

Fig. 12 shows contours of Nusselt numbers normalized by averaged Nusselt numbers on the end-wall in the upstream region (A) and downstream region (B) of the experimental

data and the present results. The upstream min, max = 0.2, 1.8 and the downstream min, max = 0.9, 1.9 of the Nusselt numbers in all the models are the same as in the experimental data presented by Ames. [3] The Nusselt number is relatively low near the inlet and high in the region of the leading edge.

The SBES results show the best agreement with the experimental data, in particular the high Nusselt number in the passage between the second row pins, and the pattern of this Nusselt number distribution in the wake region after the fifth and seventh rows. The discontinuous regions between the first row and the second row are shown in IDDES and $k-\omega$ SSTLM. The IDDES model is able to predict a similar distribution overall but there are small differences in the regions as mentioned above. The $k-\omega$ SSTLM model shows different patterns in the high-velocity passage between two symmetric rows, and the contours don't look symmetric even with enough time-averaging. Benhamadouche et al. [22] suspected the presence of very low frequencies that are not physical during solving the governing equations pertaining to non-symmetric flow patterns in the $k-\omega$ SST model. In the IDDES and $k-\omega$ SSTLM models, the Nusselt number near the leading edge of the first row increases, then slightly decreases, and then increases again, whereas the SBES model shows a gradual increase without any decreases. This can be confirmed by the local Nusselt number distributions in Fig. 12. This abnormal behavior is related to the prediction of horseshoe vortex structures near the leading edge of obstacles attached to the wall.

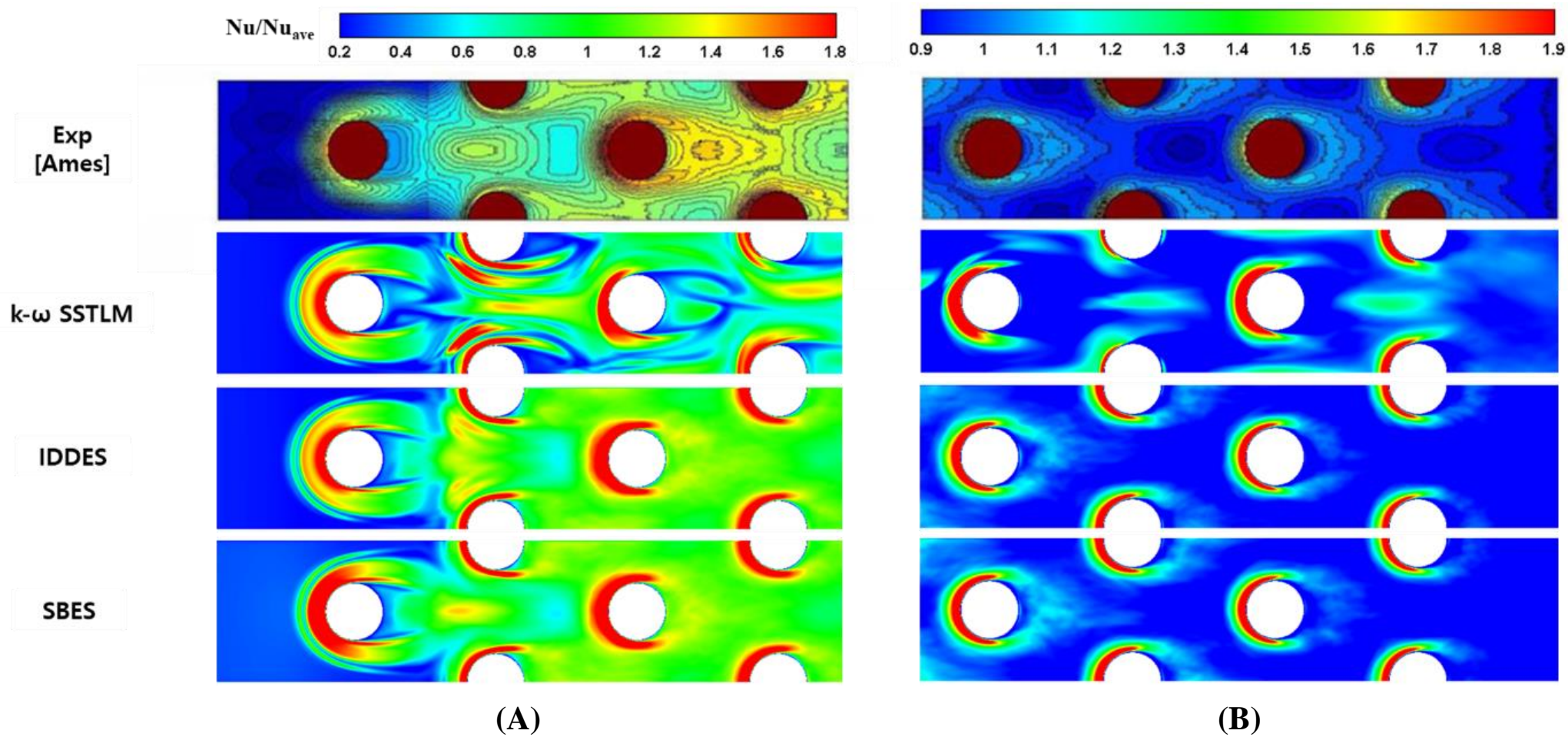


Fig. 12. Nusselt number distributions normalized by surface average Nusselt numbers. (A) Upstream region, (B) Downstream region.

4.4.9 Q-criterion

The vortical structures of instantaneous flow fields are investigated with a Q-criteria value of 10 [23] in Fig. 13. These iso-surfaces are colored by temperatures from 290 K to 315 K, and the flow field is heated gradually as the flow moves downstream. Horseshoe vortices, which are also shown in Fig. 14, can be recognized in front of the pins but it is difficult to identify them in the downstream pins. A vortex tube in the spanwise direction from each pin is generated after separation from the first pin and breaks down into 3-D vortices in the streamwise direction interacting with downstream pins. The two hybrid RANS/LES models, IDDES and SBES, are better able to resolve smaller vortex structures than the $k-\omega$ SSTLM model, as shown in Fig. 13, and they show similar structures when compared with other LES results.[4, 7] In the $k-\omega$ SSTLM model, 2-D vortices are sustained until the sixth pin, and then break into 3-D flow features that are larger than in the other models. Of particular note is that SBES is able to capture the distorted spanwise vortex tube after separation from the first pin, whereas the IDDES and $k-\omega$ SSTLM models fail to predict it even with the same grid numbers and Q-criteria value.

4.4.10 Turbulence structure

Fig. 14 shows time-averaged streamline patterns and temperature contours in the front cylinder part at the mid-line of the xz -plane. As mentioned above, the three models are able to capture the horseshoe vortex system, including HV (horseshoe vortex), SV (secondary vortex), and TV (tertiary vortex). The SBES model predicts this vortex system slightly closer to the first cylinder wall than the other two models do, and the CV (corner vortex) is shown clearly in the SBES model. It is interesting that the region where the horseshoe vortex systems are predicted is coincident with the region where the LES mode is active in the SBES model.

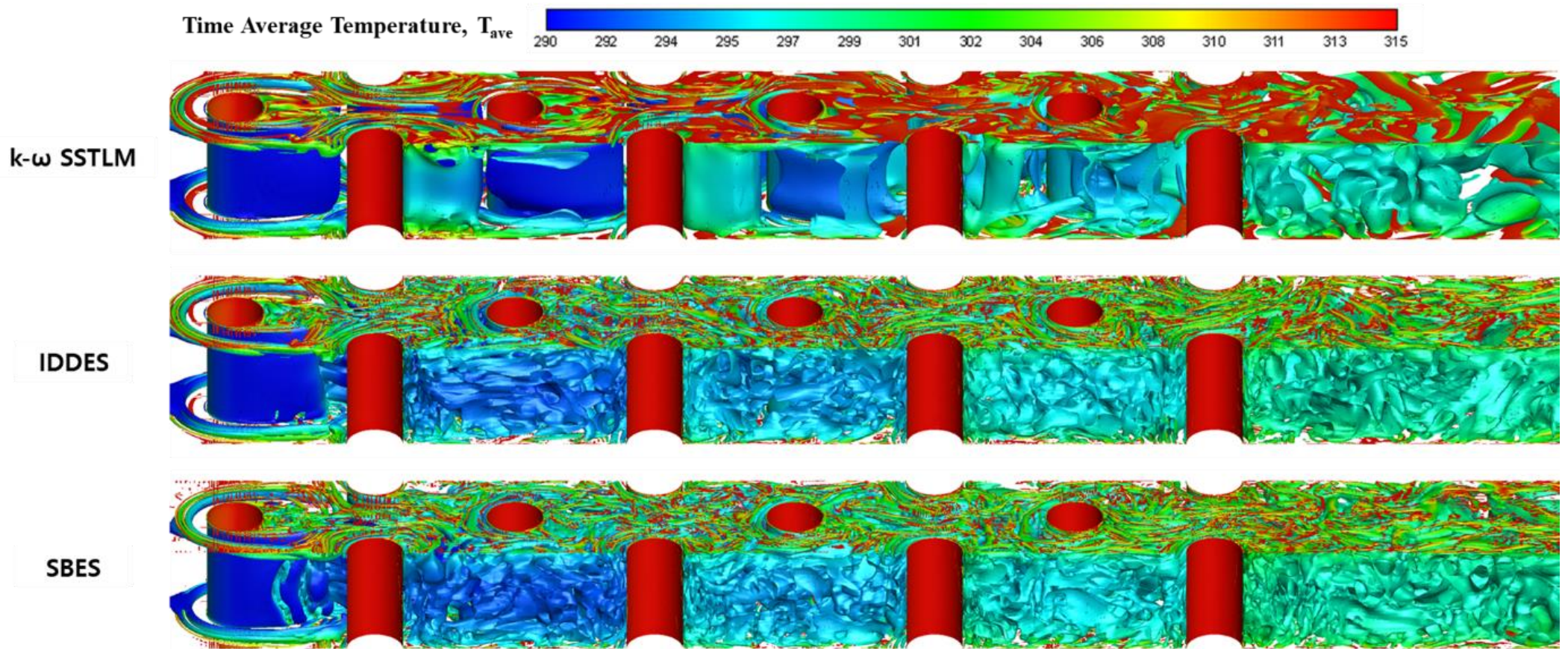
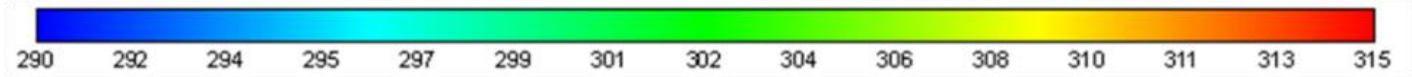
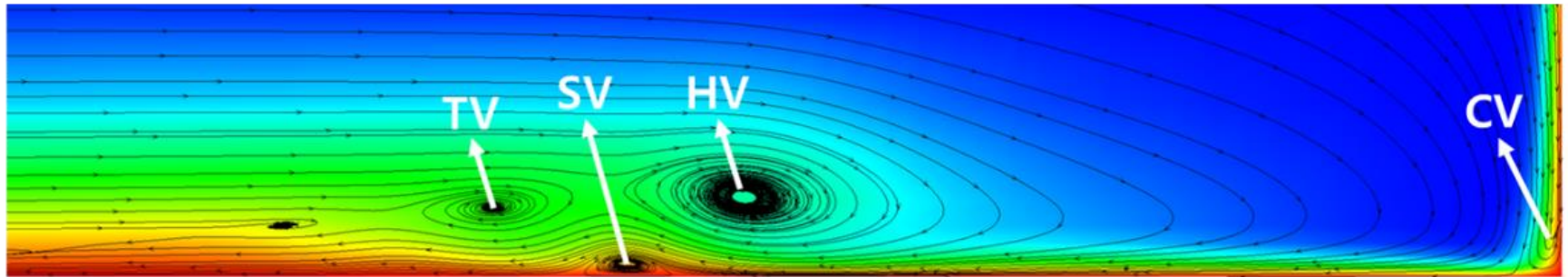


Fig. 13. Vortical structures around pin fin array, Q iso-surface ($Q=10$) colored by T_{ave} for each turbulence model.

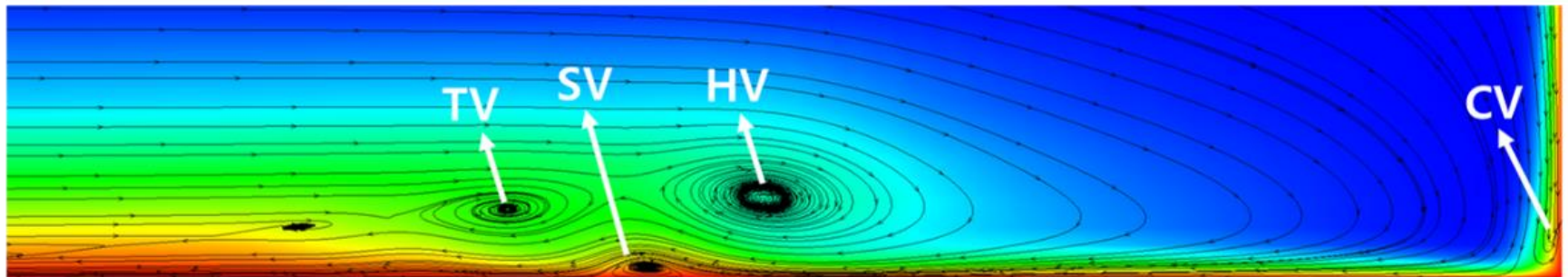
Time Average Temperature, T_{ave}



k- ω SSTLM



IDDES



SBES

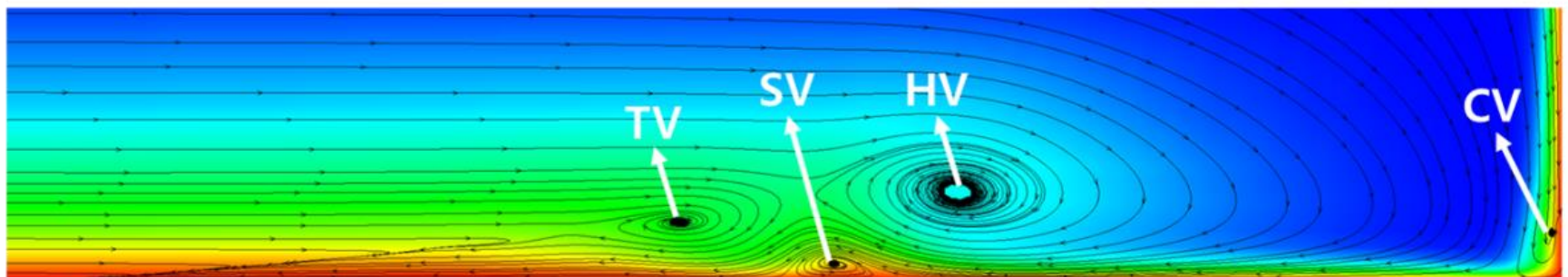


Fig. 14. Time-averaged streamlines colored by T_{ave} in front of the first row of pins. HV, horseshoe vortex; SV, secondary vortex; TV, tertiary vortex; CV, corner vortex.

4.4.11 Blending function

To investigate the effects of the blending function which changes the turbulence model between RANS and LES, the contours of the blending function are plotted in Figs. 16 and 17 with respect to two planes: the xz -plane at the mid-line of the y -axis and the xy -plane at the center height of the z -axis. The value 1 means the RANS method is adopted and 0 is for the LES method. Since the k - ω SSTLM model is not a hybrid RANS/LES method but, rather, a transitional model, the intermittency (γ) which reflects laminar flow with a 0 value and turbulent flow with 1 is contoured at the same planes. As can be seen in the two figures, the SBES model adopts the LES calculation in a larger region than that of the IDDES model, and shows a sharp transition from RANS to LES; in contrast, the IDDES model changes the two methodologies smoothly. In front of the first pin the LES calculation is changed more rapidly in the SBES model than in IDDES. This is why the results of the SBES model more closely resemble LES results than do the other models.

In the k - ω SSTLM model, as expected, flows near the inlet are predicted in laminar flow and then develop into the turbulent flow which is sustained until the outlet of the computational domain. Menter [10] mentioned that the shielding function in SBES can cover the boundary layer, including the rapid growth area by the adverse pressure gradient, while the shielding function of DDES impairs this region. In the computation domain of the present work, a total of 12 cylinders (4 cylinders at the mid-line and 8 half-cylinders at the periodic plane) experience adverse pressure gradients in the back part (approximately $\theta > 90^\circ$) of each cylinder. As seen in Figs. 16 and 17, the SBES model implies a clear and sharp RANS mode near the cylinder walls, but the IDDES model does not show a continuous and smooth transition between RANS mode and LES mode near the wall.

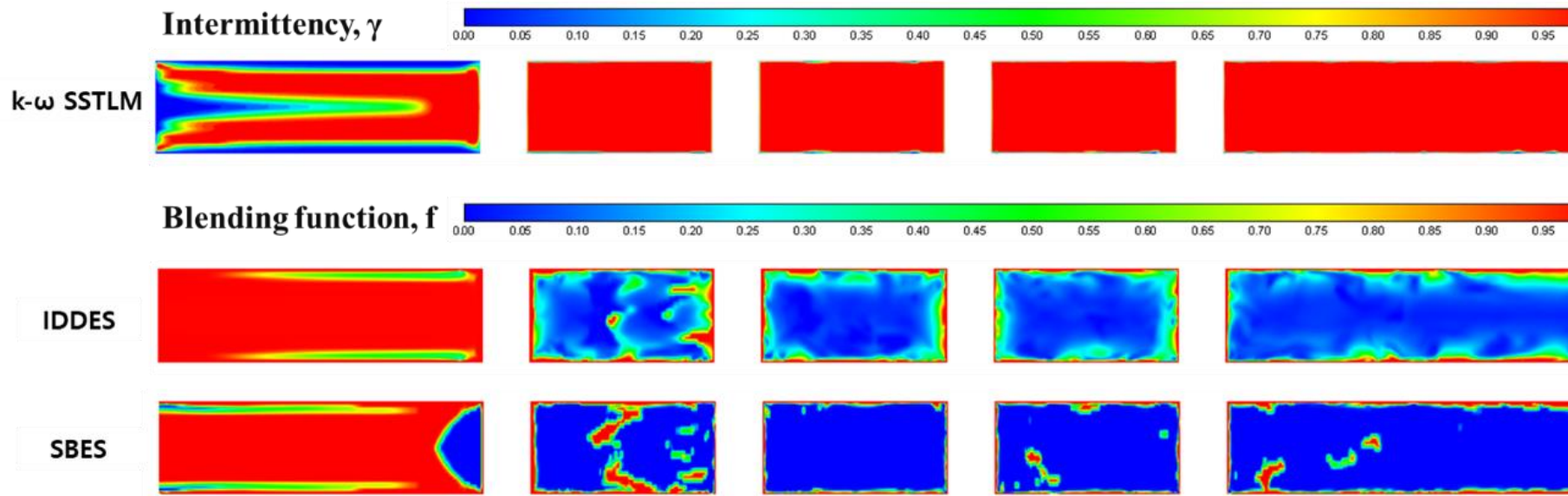


Fig. 15. Intermittency and blending function distributions on the xz -plane at the mid-line of the y -axis

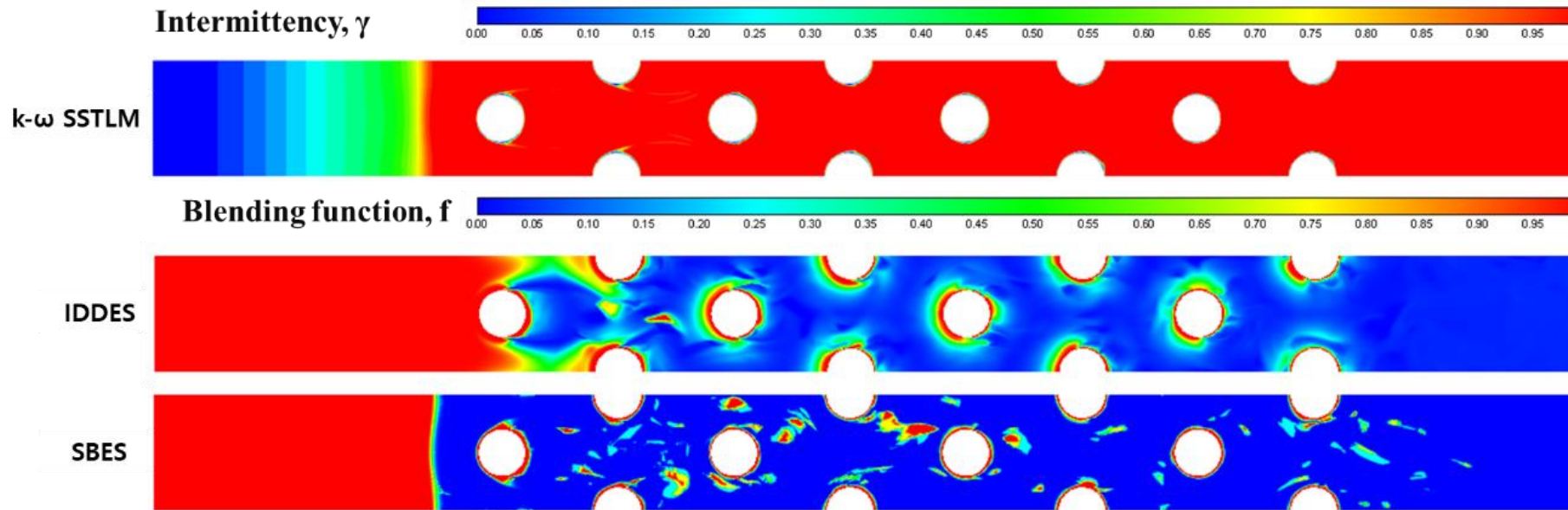


Fig. 16. Intermittency and blending function distributions on the xy -plane at the center height of the z -axis

Chapter 5. Uncertainty Quantification for Staggered Pin-Fin Arrays

5.1 gPCE results

The uncertainty quantification is conducted for staggered pin-fin arrays. The single random variable is considered in the present work. The input random variable is the inlet velocity. The probability distribution of inlet velocity is assumed as a uniform distribution and a normal distribution. The mean value μ is 3.45 m/s, and the standard deviation σ is $\pm 0.1\mu$. The quantity of interest (QoI) is Nusselt number on the endwall. Turbulence model used in uncertainty quantification is IDDES. Because IDDES has generally been used in CFD research and its source code is already opened.

For uncertainty quantification, the sample points are obtained by using Latin Hypercube sampling (LHS) method. To approximate the output probability distribution with polynomial chaos, the order of polynomial chaos p is assumed as 2nd order. Therefore, the minimum sampling points to approximate probability distribution with 2nd order are 3. Oversampling rate is set as 2. [25] Total 6 sample points are used in uncertainty quantification. The table 5 shows the value of each sample points and QoI. From the sample points, the polynomial chaos coefficients are calculated and shown in Table 6.

Table 5. *The sampling points and output values*

	Point1	Point2	Point3	Point4	Point5	Point6
Inlet velocity [m/s]	3.21650	3.28000	3.44088	3.50785	3.59867	3.76215
Nu_{ave}	41.62	42.15	43.07	43.68	44.05	45.16

Table 6. the polynomial chaos coefficients depending on probability distribution of input parameter

coefficient	a_0	a_1	a_2
Uniform distribution	43.1715	1.2790	-0.0227
Normal distribution	43.1208	2.2153	-0.1075

Fig. 17 shows the probability density function (PDF) of average Nusselt number. These PDFs are generated from the surrogate model based on 30,000 random sampling points. The probability distribution of input parameter affects the probability density function (PDF) of average Nusselt number. (A) shows PDF of average Nusselt number when the input PDF is the uniform distribution. Its mean μ is 43.1714 and the standard deviation σ is 1.2792. (B) shows the PDF of average Nusselt number when the input PDF is normal distribution. Its mean μ is 43.1208 and the standard deviation σ 2.2179. These results show that only the assumption about the input variable's probability distribution induces totally different result distribution.

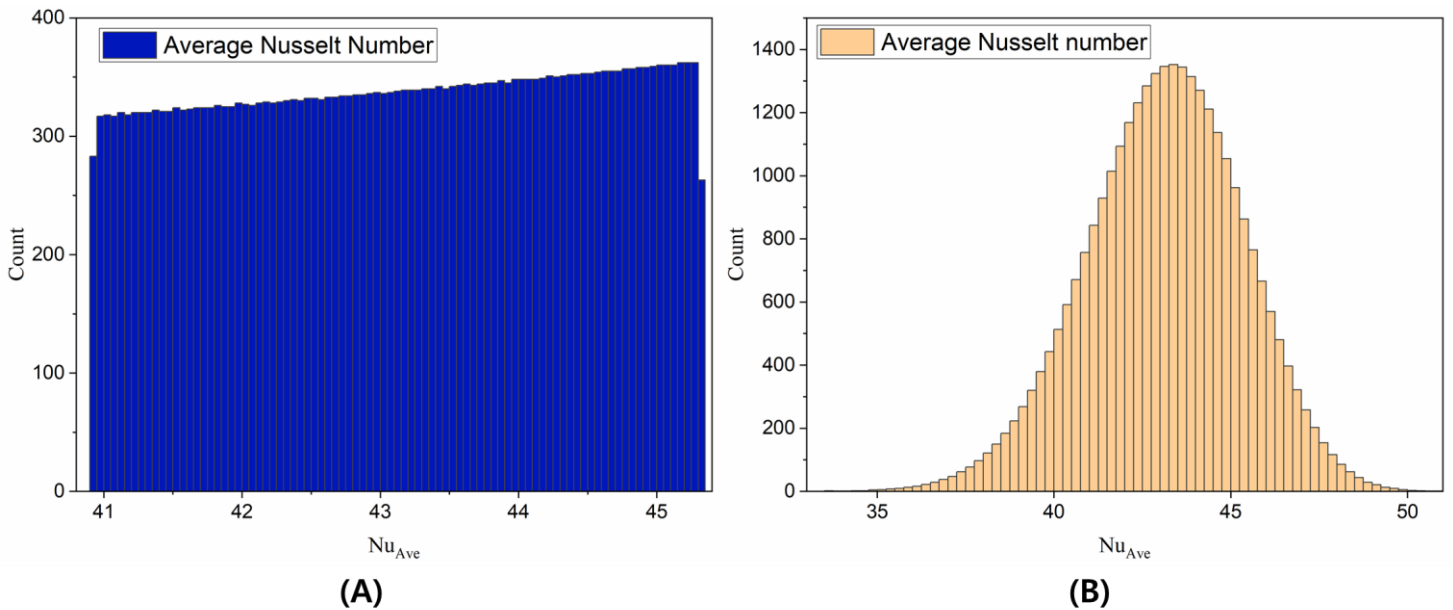


Fig. 3. Histogram of the average Nusselt number depending on the input random distribution. (A) Uniform distribution, (B) Normal distribution.

Fig.18 shows that the box and whisker plot of the local Nusselt number along the middle line on the endwall depending on the input variable's probability distribution. (A) is the result of the uniform distribution and (B) is the result of the normal distribution. The mean value and standard distribution of each input probability distribution are the same with the average Nusselt number results. The 10 points are considered to quantify the uncertainty between each pin. Therefore, 40 points are considered totally. The mean value results of the uniform distribution and the normal distribution show similar with the deterministic results of Nusselt number distribution shown in Fig.11. Both results show that the propagation of the uncertainty decrease in moving downstream. This tendency is significant in the results of uniform distribution especially. In addition, the uncertainty is high near the pin. However, the results of normal distribution show larger uncertainty than the results of uniform distribution.

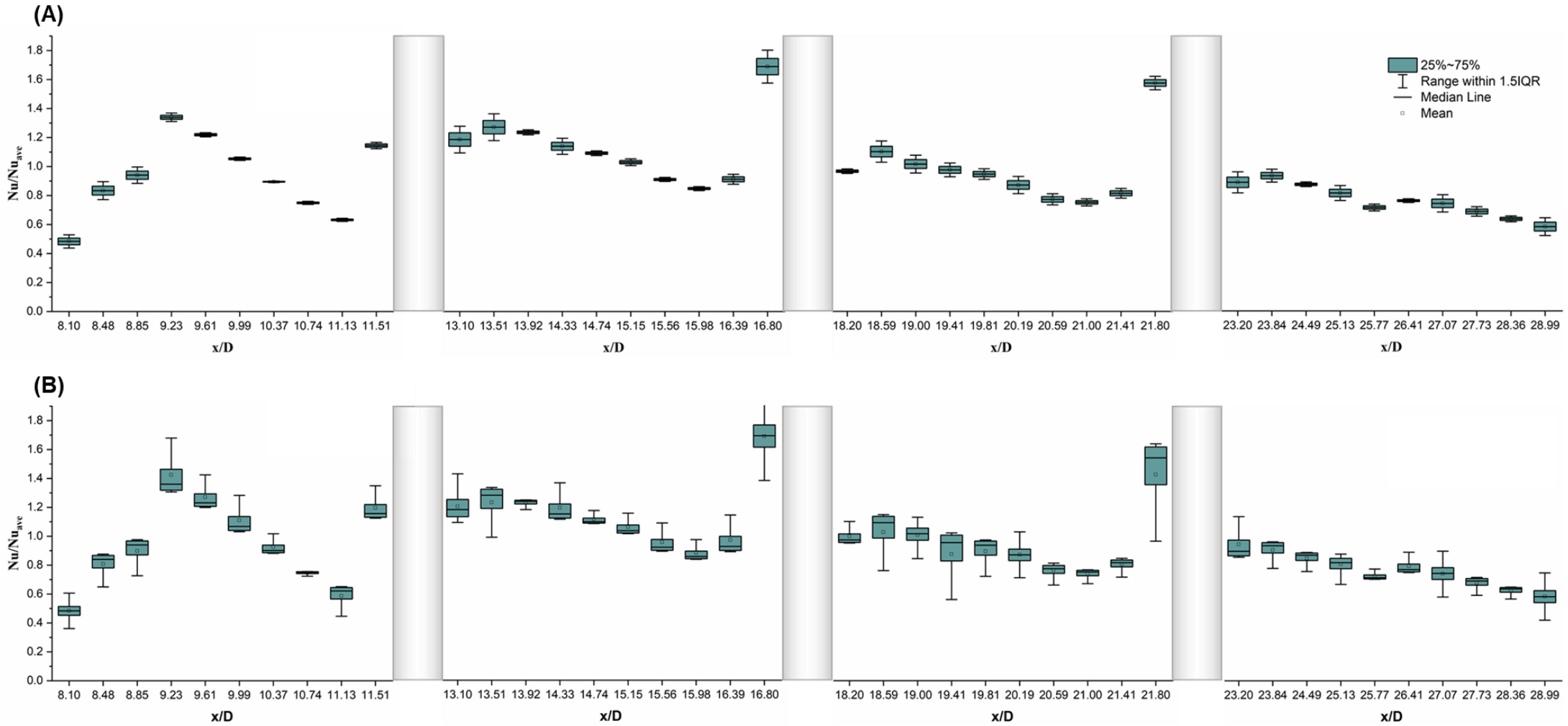
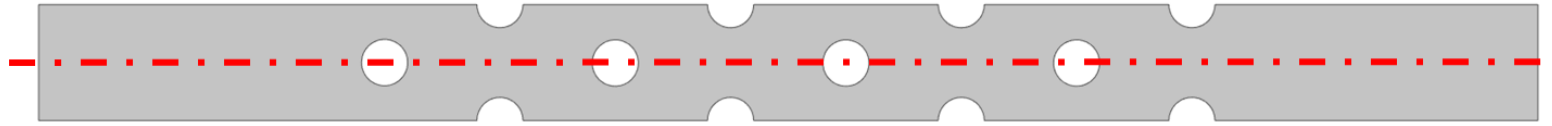


Fig. 4. Histogram of the local Nusselt number along the middle line depending on the input random distribution. (A) Uniform distribution, (B) Normal distribution.

Chapter 6. Conclusion

6.1 Conclusions

In the present work, two hybrid RANS/LES modes, IDDES and SBES, and one transitional URANS model, $k-\omega$ SSTLM, are adopted to investigate their ability to predict heat and fluid flow phenomena around staggered pin-fin arrays. The corresponding Reynolds number based on the pin diameter and the maximum velocity between the pins is 10,000, and the periodic segment geometry with a total of eight pins is considered. The simulated results, including mean velocity, pressure, local and global Nusselt numbers, and coherent structures, are compared with experimental data [1, 2, 3] and other LES [4] and URANS [5] results.

Mean velocity profiles predicted by IDDES and SBES agree well with the reference data, but the $k-\omega$ SSTLM model shows large discrepancies near the centers between the pins. In averaged pressure coefficients around the pins, the SBES model gives the closest prediction in the region of the attached flow and after the separation point, compared to all the other models in the present work. The results of the $k-\omega$ SSTLM model are similar with those of the other URANS model, the ζ -f model [5], with large discrepancies in the separated region.

The two hybrid RANS/LES models show superior predictions of the nonlinear behavior of local Nusselt numbers, with abrupt increases near the upstream of each pin and gradual decreases after the downstream wall. However, in the region downstream of the pins they slightly underestimate the local Nusselt number because they do not resolve the vortex shedding after the pins fully. In the $k-\omega$ SSTLM model the transitional behavior around the first pin is predicted well but there are large discrepancies around the other pins, the same as with the other URANS model. Similarly, the two hybrid RANS/LES models predict the

distributions of Nusselt numbers around the pins and the averaged Nusselt number in each section of pins, very similar to the other LES results.

Vortical structures, including horseshoe vortex systems in front of the first pin and wakes after each pin, are fully resolved in the two hybrid RANS/LES models, very similar to the LES model. In particular, the SBES model is able to capture the distorted spanwise vortex tube after separation from the first fin, whereas IDDES and $k-\omega$ SSTLM fail based on the same grid system.

In our investigation of the effects of the blending function of the two hybrid RANS/LES models, the SBES model adopts the LES calculation in a larger region with a sharp transition from RANS to LES, compared to the IDDES model. Therefore, the SBES prediction more closely resembles the LES results.

Uncertainty Quantification is conducted by varying the PDF of the inlet velocity. The average Nusselt number PDF shows the similar distribution with input parameter PDF. When the input PDF is uniform distribution, the mean μ of the output PDF is 43.1714 and standard deviation σ is 1.2792. When the input PDF is normal distribution, the mean μ of the output PDF is 43.1208 and standard deviation σ is 2.2179. The local Nusselt number also investigated by using uncertainty quantification. It's median value distribution is similar with the deterministic solution of local Nusselt number. However, the uncertainty distribution is different. Especially normal distribution show high uncertainty. from the results, aleatory uncertainty is quantified. The input probability distribution induces different the output probability distribution.

6.2 Future works

From the results of the uncertainty quantification, we can conclude that the credible results can be obtained by applying the exact input probability distribution. The future works are needed to identify the input probability distribution with Bayesian inference. For Bayesian inference, the observation data is needed. the experimental data or LES simulation results can be observation data. Therefore, LES simulation will be conducted for comparing the results of other turbulence model and the results of LES simulation also can be used with observation data in Bayesian inference.

REFERENCES

1. Ames, F.E., Dvorak, L.A., Morrow, M.J., 2005. Turbulent augmentation of internal convection over pins in staggered-pin fin arrays. *J. Turbomach.* 127 (1), pp.183-190
2. Ames, F.E., Dvorak, L.A., 2006, Turbulent transport in pin fin arrays: experimental data and predictions. *J. Turbomach.* 128 (1), pp.71-81
3. Ames, F.E., Nordquist, C.A., Klennert, L.A., 2007. Endwall Heat Transfer Measurements in a Staggered Pin Fin Array with an Adiabatic Pin. ASME Paper No. GT2007-27432.
4. Delibra, G., Borello, D., Hanjalic, K., Rispoli, F., 2008. LES of Heat Transfer in a Channel with a Staggered Pin Matrix. Direct and Large-Eddy Simulation VII, Proceedings of 7th International ERCOFTAC Workshop, Trieste. Springer Science and Media BV. pp. 9-10.
5. Delibra, G., Borello, D., Hanjalic, K., Rispoli, F., 2009. URANS of flow and endwall heat transfer in a pinned passage relevant to gas-turbine blade cooling. *Int. J. Heat Fluid Flow* 30 (3), pp.549-560.
6. Delibra, G., Borello, D., Hanjalic, K., Rispoli, F., 2010. Vortex structures and heat transfer in a wall-bounded pin matrix: LES with a RANS wall-treatment. *Int. J. Heat Fluid Flow* 31 (5), pp.740-753.
7. Hao, Z., Gorle, C., 2019. Large eddy simulation of forced heat convection in a pin-fin array with a priori examination of an eddy-viscosity turbulence model. *Int. J. Heat Fluid Flow* (77), pp.73-83.
8. Carnevale, M., Montomoli, F., D'Amico, A., Salvadori, S., Martelli, F., 2013. Uncertainty quantification: a stochastic method for heat transfer prediction using LES. *J. Turbomach.* 135 (5), 051021.
9. Spalart, P. R., Jou, W. H., Strelets, M., Allmaras S. R., 1997. Comments on the feasibility of LES for wings, and on a Hybrid RANS/LES approach. 1st AFOSR Int. Symp. Eng. Turb. Modeling and Measurements, pp 24-26.

10. Menter, F., 2018. Stress-Blended Eddy Simulation (SBES)- A New Paradigm in Hybrid RANS-LES Modeling. Symposium on Hybrid RANS-LES Methods, Cham, Springer, pp.27-37.
11. Frank, T., Menter, F., 2017. (PDF) Validation of URANS SST and SBES in ANSYS CFD for the turbulent mixing of two parallel planer water jets impinging on a stationary pool. ASME 2017 verification and validation symposium.
12. Syawitri, T. P., Yao, Y. F., Yao, J., Chandra, B., 2019. Assessment of stress-blended eddy simulation model for accurate prediction of three-straight-bladed vertical axis wind turbine performance. 54th 3AF International Conference on Applied Aerodynamics, Paris, France
13. Lengry, R.B., Menter, F.R., 2009, Correlation-based transition modeling for unstructured parallelized computational fluid dynamics Codes. AIAA J. 47, pp.2894.2906.
14. ANSYS, 2017, ANSYS Fluent Theory Guide. <http://www.ansys.com/>
15. ANSYS, 2017, ANSYS ICEM CFD User's Manual . <http://www.ansys.com/>
16. Gritskevich, M.S., Garbaruk, A.V., Schutze, J., Menter, F.R., 2012. Development of DDES and IDDES Formulations for the k- ω shear Stress Transport Model. Int. J. Flow Turbulence Combust (88), pp.431-449.
17. Spalart, P. R., Deck, S., Shur, M. L., Squires, K. D., Strelets, M. K., Travin, A., 2006. A new version of detached-eddy simulation, resistant to ambiguous grid densities. Theoretical and computational fluid dynamics 20 (3), p.181
18. Shur, M. L., Spalart, P. R., Strelets, M. K., Travin, A. K., 2008. A Hybrid RANS-LES approach with delayed-DES and wall-modeled LES capabilities. Int. J. Heat Fluid Flow 29, pp.1638-1649.
19. Piomelli, U., Balaras, E., 2002. Wall-layer models for large-eddy simulations. Annual review of fluid mechanics 34(1), pp.349-374.
20. Menter, F. R., 1994. Two-equation eddy-viscosity turbulence models for engineering applications. AIAA journal 32 (8), pp. 1598-1605.

21. Nikitin, N. V., Nicoud, F., Wasistho, B., Squires, K.D., Spalart, P. R., 2000, An approach to wall modeling in large-eddy simulations. *Physics of fluids* 12 (7), pp. 1629-1632.
22. Benhamadouche, S., Afgan, I., Manceau, R., 2019. Numerical simulations of flow and heat transfer in a wall-bounded pin matrix. *Int. J. Flow Turbulence Combust* 104 (1), pp.19-44.
23. Dubief, Y., Delcayre, F., 2000. On coherent-vortex identification in turbulence. *J. turbulence* 1(1), pp.11-11.
24. McKay, M. D., Schiller, S. B., and Welch, W. J., 1979, A comparison of three methods for selecting values of input variables in the analysis of output from a computer code, *Technometrics*, Vol. 31, No. 1, pp.41-47.
25. Hosder, S., Walters, R., Balch, M., 2007, Efficient sampling for non-intrusive polynomial chaos applications with multiple uncertain input variables, 48th AIAA/ASME/ASCE/AHS/ASC Structures, Structural Dynamics, and Materials conference, Honolulu, Hawaii, USA, AIAA 2007-1939.